Attenuation of seismic shear wave energy in Switzerland

Geophysical Journal International

Geophys. J. Int. (2011) **185,** 967–984 doi: 10.1111/j.1365-246X.2011.04987.x

Attenuation of seismic shear wave energy in Switzerland

Benjamin Edwards, Donat Fäh and Domenico Giardini

Swiss Seismological Service, Sonneggstrasse 5, 8092 Zürich, Switzerland. E-mail: edwards@sed.ethz.ch

Accepted 2011 February 11. Received 2011 February 11; in original form 2010 October 28

SUMMARY

Modelling the attenuation of shear wave energy is an important component of seismic hazard analysis. Previous studies have shown how attenuation, particularly in the uppermost layers of the crust, is regionally dependent. The impact of this is that the decay of energy radiating from an earthquake will vary from place to place. To quantify the regional attenuation in Switzerland we model the Fourier spectral amplitude of small-to-moderate earthquakes, recorded on the local seismic networks. High-frequency decay is parametrized by Q and κ, while apparent geometrical spreading models account for the frequency-independent decay of energy. We analyse ground motion encompassing the significant duration of shaking to provide models that are useful for the purpose of seismic hazard analysis. Two methods are used to estimate the whole path attenuation parameter, t^*: first, a simultaneous fit of the source model and attenuation effects across the entire spectral bandwidth for earthquakes with $M > 2$; and secondly, a linear fit of an attenuation model to the high-frequency part of the spectrum for earthquakes with $M > 3.5$. The t^* parameter is found to vary with hypocentral distance consistent with a weakly attenuating crust and strongly attenuating uppermost layer. 1-D tomographic inversions indicate a profile of increasing Q with depth down to the Moho. Frequency-independent decay is parametrized using a three-part model which allows for the inclusion of Moho reflection phases in the spectrum in the range of 20–140 km in the Swiss Foreland and from 70 to 140 km in the Swiss Alps.

Key words: Fourier analysis; Earthquake ground motions; Seismic attenuation; Seismic tomography; Europe.

1 INTRODUCTION

The characterization of shear wave energy attenuation is an important aspect of seismic hazard analysis. Q and κ, the parameters describing the degree of attenuation along the propagation path are a critical input of stochastic models, often used for ground-motion prediction in regions of low-to-moderate seismicity (e.g. Toro *et al*. 1997; Atkinson & Boore, 2006). However, well-documented trade-offs between source-, path- and site parameters means that their decoupling is non-trivial (e.g. Boore *et al*. 1992; Bay *et al*. 2003; Ide *et al*. 2003; Edwards *et al*. 2008).

Bay *et al*. (2003, 2005) presented a model of shear wave attenuation in Switzerland based on band-limited data recorded on short-period instrumentation with frequency modulation (FM)-telemetry. They modelled restituted spectra up to 12 Hz, decoupling the source-, path- and site effects. The strongly limited bandwidth of recording, in addition to potentially unknown recording and analogue transmission effects, could lead to bias or high uncertainty in the resulting parameters. However, since 1998–2002, the Swiss Seismological Service (SED) has been operating fully digital broad-band and strong-motion online seismic networks (Fig. 1): the Swiss Digital Seismic Network (SDSNet) and the Swiss Strong Motion Network (SMSNet), respectively. A significant quantity of high-quality data has therefore been obtained since the Bay *et al*. (2003) study.

In this study we aim to robustly characterize shear wave attenuation using the new digital data. An emphasis on the description of attenuation in terms of data constituting the significant duration of shaking is made. This facilitates the attenuation model's subsequent usage in stochastic modelling. To address the issue of parameter trade-off we test two methods to estimate the t^* parameter: a simultaneous fitting method, which benefits from numerous data available and a linear fit of high-frequency data from $M >$ 3.5 events (following Anderson & Hough 1984). The latter is less susceptible to the trade-off between source and site, but limited by the low quantity of data available.

Using the new t^* values, we use different methods to model the data with a homogeneous Q_0 and site-specific κ: a bootstrap approach to limit the effect of biased data distribution, and a matrix inversion to limit the effect of individual stations on the attenuation model. An alternative way to describe the crustal and near surface attenuation structure is to use a tomographic modelling approach (e.g. Rietbrock 2001; Edwards *et al.* 2008; Eberhart-Phillips *et al*. 2008, 2010; Edwards & Rietbrock 2009). In this study we model the 1-D attenuation profiles of two characteristic regions, the Swiss Foreland and the Alps. Finally, the apparent geometrical spreading

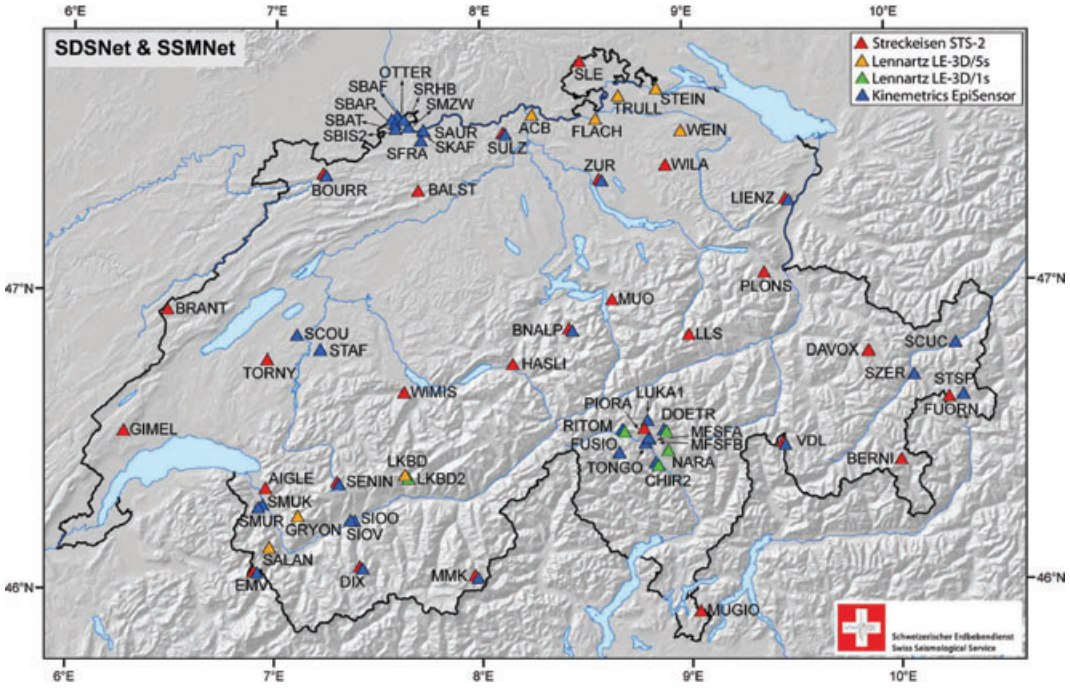

Figure 1. Real-time stations of the Swiss Digital Seismic Network (SDSNet) and the Swiss Strong Motion Network (SMSNet) used in this study.

(Atkinson & Mereu 1992; Edwards *et al*. 2008) of energy is quantified. The model accounts for geometrical effects, scattering and focusing, in addition to phase inclusion (such as the Moho reflection phase: SmS).

2 DATA COLLECTION

High-quality broad- and medium-band recordings from SDSNet and SMSNet were collected for this analysis. The recordings span a time period between 1998 and 2009. Due to concern over the validity of the instrument response function for the older short period and FM-telemetry instrumentation these data (e.g. Bay *et al*. 2003) were not used. The majority of recordings in our data set were made on broad-band STS-2 seismometers, with further recordings on 5 s Lennartz seismometers and Episensor accelerometers (Deichmann *et al*. 2010). Instrumental coverage was increased by collecting digital broad-band data from selected networks of neighbouring countries (see Acknowledgements).

All events occurring between 1998 and 2009, with $M_L \geq 2.0$, and located by the SED within the following coordinates (zone 1), are included in the data set

Latitude range: 5°50′E to 10°40′E;

Longitude range: 45°40′N to 48°00′N.

Earthquakes occurring in the locality of Switzerland are all crustal earthquakes (depths of no greater than around 30–40 km in the Foreland and 15–20 km in the Alpine region). The data set defined here is also used in a companion study of ground-motion scaling; to extend the data set at the upper end of the magnitude scale we therefore expanded the acceptable epicentre location area (zone 2) for magnitudes $M_L{}^{SED} \geq 4.0$ to

Latitude range: 5°00′E to 11°30′E;

Longitude range: 45°00′N to 48°30′N

Both zones along with all included events are shown in Fig. 2. A distinction between Foreland and Alpine regions is quantified through the line

$$\text{Latitude} = 0.4(\text{Longitude} - 6.0^{\circ}) + 45.8^{\circ}, \quad (1)$$

where the Foreland region is to the north and Alpine region to the south.

2.1 Data processing

The data selection and processing follows the approach used by Edwards *et al*. (2010). Waveforms are first windowed to provide data that are categorized as signal and noise, one of each being necessary for each record. If *S*-wave arrivals are not available, a *P*:*S* ratio of 1.73 is used to estimate the arrival time from manual *P*-wave picks. The signal window duration and position are based on the method proposed by Raoof *et al*. (1999) to encapsulate 5 per cent to 75 per cent of the cumulative squared velocity of the record (a measure of the duration of significant shaking). The use of signal windows based on the duration of shaking is driven by the consideration of future applications in seismic hazard. The approach also has the advantage that the results are relatively insensitive to the pick-times of the *P* and *S* waves, and in addition, provides a quantitative measure of shaking duration based on the cumulative squared velocity for further analysis.

Following the selection of the signal-window, a pre-P-wave noise window is selected. The window starts at the beginning of the trace, and continues over a duration equal to 75 per cent of the time until the *P*-wave arrival. This ensures that potentially inaccurate *P*-wave arrival time picks (or estimates) do not lead to the noise window being contaminated by the *P* arrival. Both signal and noise windows (excluding the zero padding) are demeaned and tapered using multitaper algorithms (Park *et al*. 1987; Lees & Park 1995) with five 3π-prolate tapers, before applying a fast Fourier transform (FFT) and multiplying by the sampling period to obtain the two-sided continuous Fourier velocity spectrum of each record. To account for different window lengths used for the signal and noise spectra

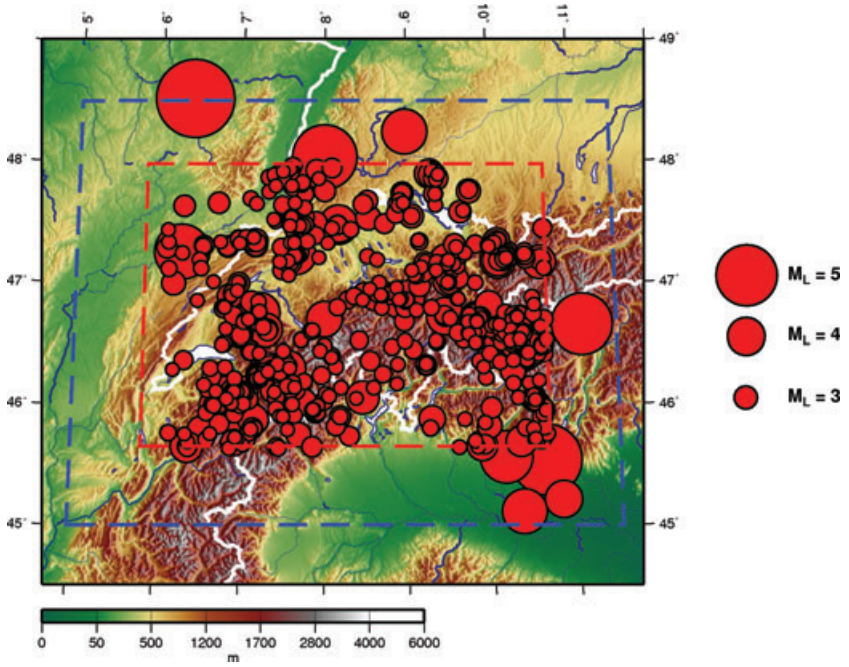

Figure 2. Topographical map of Switzerland and border regions showing events included in the data set. The dashed red rectangle shows zone 1 and the dashed blue rectangle shows zone 2 as referred to in the text.

the noise spectra are also normalized by $N_{\text{signal}}/N_{\text{noise}}$, where N is the number of points in the time-series (excluding the zero-padding). For accelerometric records the spectral data are integrated by dividing by iω. All data are then corrected to records of ground-velocity through deconvolution with the instrument response function (using the poles and zeros). Note that the same inversion process is later applied to data recorded on both velocimeters and accelerometers. The signal-to-noise ratio analysis selectively defines the valid frequency range for each individual recording, which takes into account the different instrument sensitivities. We often see, for instance, that at colocated velocimeters and accelerometers, the valid frequency range is at lower frequencies on the velocimeter, and higher frequencies on the accelerometer.

To extract only the most reliable data, the noise estimate is conservatively increased to insure concurrence of the signal and noise at both the lowest (e.g. 0.01 Hz) and highest (e.g. 50 Hz) available frequencies of each spectrum. While this may reduce the available bandwidth above the signal-to-noise ratio, it prevents unwanted effects from being included in the data. For example, effects due to the high variance of low-frequency spectral levels for relatively short window lengths, and the time-variance of noise. The useful frequency range is then defined for each recording as where the signal-to-noise ratio is greater than 3 over a continuous bandwidth of at least 1 $\log_{10}$ units of frequency (e.g. 1–10 Hz, 0.5–5 Hz, etc). Cut-off limits for the maximum 'low-frequency' and minimum 'high-frequency' of the spectra are defined as 5 and 10 Hz, respectively, such that spectra starting at frequencies greater than 5 Hz, or ending before 10 Hz are discarded.

2.1.1 Overall data coverage and statistics

A total of 720 earthquakes were available after quality control processing, with 18 308 individual horizontal records (N–S or E–W). Fig. 2 shows the distribution of events with respect to their size. It can be seen that most events are $M_L < 3$ and the larger events tend to occur on the borders of the study region. The Foreland region has deeper events than the Alpine region, but depths do not vary systematically with longitude. The depth of event versus hypocentral distance to recording station (r) shows relatively uniform coverage.

Fig. 3 shows statistics of the data available to the inversions after quality control. Fig. 3(a) shows that the majority of spectra have frequency bandwidths of 0.8–30 Hz. The minimum frequency is distributed approximately log-normally. The minimum 'low-frequency limit' is just over 0.1 Hz. The maximum 'low-frequency limit' is less than 2 Hz. For the maximum frequency available in the spectra, there was a limit of 30 Hz. Over 50 per cent of the spectra pass the quality control even up to this maximum frequency. The minimum 'high-frequency limit' is 10 Hz. Figs 3(b) and (c) show that the distribution of event magnitude against event recording distance is rather uniform, especially considering the implication of noise at low levels of ground motion for distant recordings of low-magnitude events. Larger events tend to be recorded further away. This is simply due to their low rate of occurrence combined with the fact that they tended to occur at the edge of the network. Fig. 3(c) shows that there is no obvious relation between event magnitude and depth. The deepest events are located at just over 30 km.

3 ATTENUATION MODEL AND OBTAINING t^*

The attenuation of seismic energy between its source and the receiver can be quantified by the parameter t^*. Higher t^* indicates higher levels of attenuation, which can be due to a more attenuating propagation medium, or a longer period of time that the ray path spends in the propagation medium. The t* parameter along the ray path is given by:

$$t^*_{path} = \int_{r=0}^{R} \frac{\mathrm{d}r}{Q(x,y,z)\beta(x,y,z)}, \tag{2}$$

where x, y and z represent the Cartesian location along the ray path, r is the distance travelled, R is the path length, Q is the quality

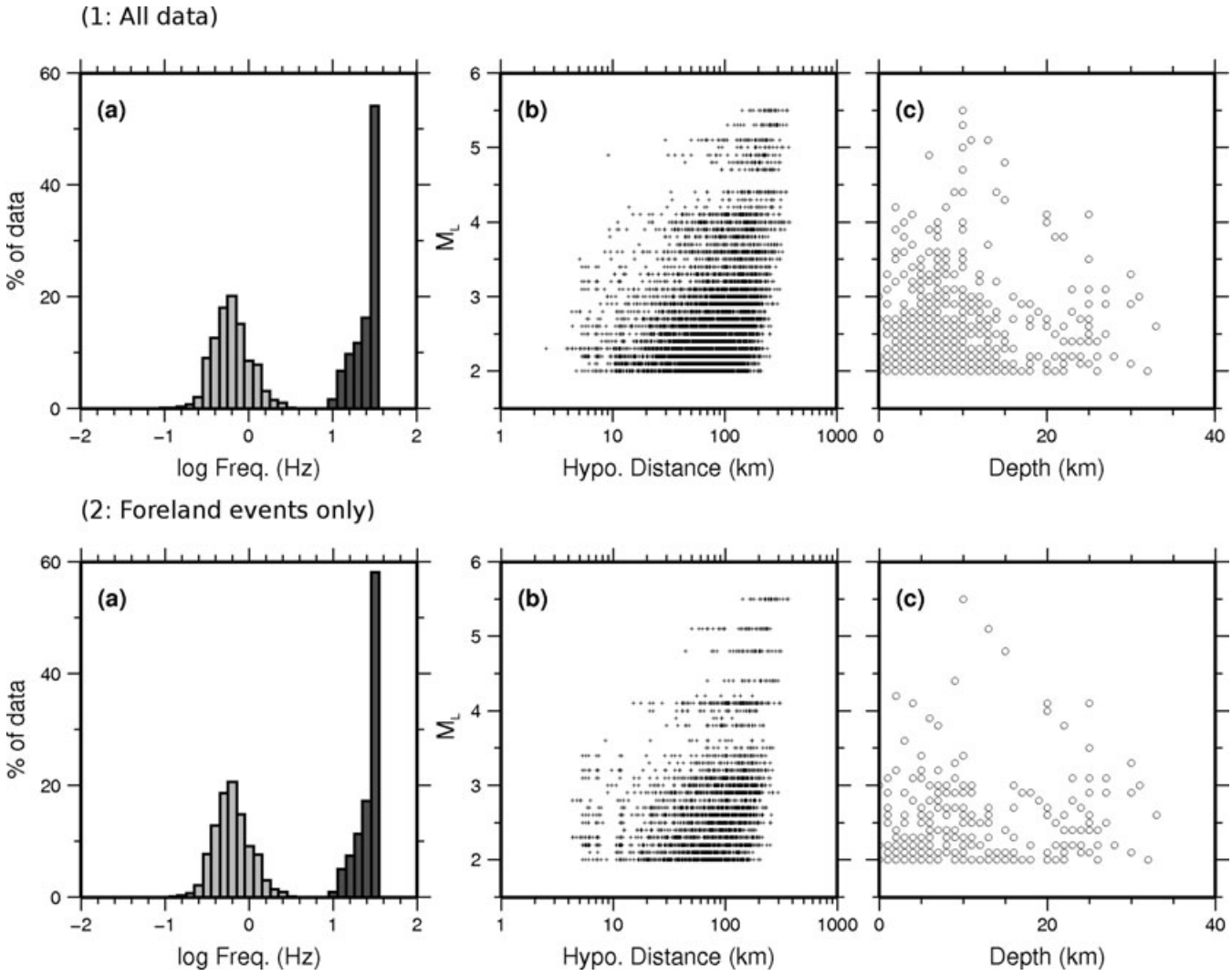

Figure 3. Data statistics: (1) all data; (2) only Foreland data; (a) plot of frequency bandwidth of spectra: minimum frequency available above noise level (light grey) and maximum frequency (up to 30 Hz) above noise level (dark grey) (the available bandwidth lies between the two histograms); (b) magnitude against hypocentral distance and (c) magnitude against depth. These data are those available after all quality control procedures have been passed. The data displayed therefore represent all those available to the inversions.

factor and β is the shear wave velocity. Some authors find that Q is dependent on frequency (e.g. Malagnini *et al*. 2000; Bay *et al*. 2003; Drouet *et al*. 2010). Typically this is parametrized as

$$Q(f) = Q_0 f^{\alpha}, \tag{3}$$

where α ranges from 0 (frequency-independent Q) to 0.9 and Q_0 is the reference value of Q at 1 Hz. There is, however a strong trade-off of the parameter α with the exponent of geometrical decay, λ: in fact for $\alpha = 1$, there is no resolution between the two (Edwards *et al*. 2008; Morozov *et al*. 2008). Previous studies of attenuation in Switzerland (Bay *et al*. 2003, 2005) found that

$$Q(f) = 270 f^{0.5}, \tag{4}$$

for a homogeneous medium with a shear wave velocity of $\beta = 3500$ m s^{-1}, along with a site-specific average κ value of 0.0125 s (in the form of Anderson & Hough 1984).

3.1 Computation of t^* estimates

3.1.1 Simultaneous broad-band spectral fit

We use two methods to compute t^*_{path}. The first follows Edwards *et al*. (2008) and Edwards & Rietbrock (2009). This method was based on Scherbaum (1990) and Rietbrock (2001) and uses broad-band spectral fitting to estimate t^*_{path}. The following model of the Fourier velocity spectrum is assumed:

$$\Omega_{ij}(f, r) = C_{ij} f E_i(f, f_{ci}) B_{ij}\left(f, t^*_{\text{path}}, \alpha\right) T_j(f), \tag{5}$$

where f is the frequency, r is the hypocentral distance and i and j represent the ith source and jth station, respectively. C_{ij} is a frequency-independent factor that is dependent on the seismic moment and phenomena such as geometrical spreading. $E_i(f,f_{ci})$ is the normalized (Brune 1970, 1971) source model with a defining corner frequency f_{ci}.

$$E_i(f, f_{ci}) = \frac{1}{\left(1 + \left(\frac{f}{f_{ci}}\right)^2\right)}. \tag{6}$$

Table 1. Generic rock amplification function from Poggi *et al.* (2011).

Frequency	Amplitude
0.10	1.01
0.20	1.03
0.40	1.10
0.80	1.31
1.60	1.62
3.20	1.75
6.42	1.78
11.97	1.79
30.00	1.82

$B_{ij}(f, t^*_{\text{path}}, \alpha)$ is the attenuation along the ray path

$$B_{ij}\left(f, t^*_{\text{path}}, \alpha\right) = \mathrm{e}^{-\pi f^{1-\alpha} t^*_{\text{path}}}, \tag{7}$$

with frequency dependence of Q defined by α, and t^*_{path} given by eq. (2). The site amplification function, $T_j(f)$, is accounted for by removing the generic Swiss rock amplification function defined by Poggi *et al*. (2011) (Table 1).

For inclusion in the spectral inversion only frequencies up to 30 Hz are considered in this case. The inversion of the spectra is performed for three defining parameters—the source corner frequency (f_c) of the Brune (1970, 1971) far-field source spectrum, the signal moment ($C_{ij}/2\pi$) and t^*_{path} using a combined grid-search for f_c and Powell's minimization for t^*_{path} and the signal moment (Press *et al.* 1997). The grid search of f_c is performed at 10 per cent intervals, starting at the equivalent f_c for a stress drop ($\Delta\sigma$) of approximately 0.001 MPa and increasing to the equivalent f_c for a 100 MPa stress drop, such that the nth grid-search f_c is given by

$$f_{c,n} = 1.1^n (0.4906\beta(\Delta\sigma_{\min}/10^{(1.5\,M_{\text{W}}+9.1)})^{1/3}, \tag{8}$$

while

$$f_{c,n} = 1.1^n (0.4906\beta(\sigma_{\max}/10^{(1.5\,M_{\text{W}}+9.1)})^{1/3}, \tag{9}$$

with $\Delta\sigma_{\min} = 0.001$ Mpa, $\Delta\sigma_{\max} = 100$ Mpa and $\beta = 3500$ m s^{-1} (Eshelby 1957; Brune 1970, 1971). M_{W} is estimated from M_{L} using the conversion relation defined by Edwards *et al*. (2010). Each earthquake is assumed to have a common corner frequency across all recordings, which is a reasonable assumption in the case of long analysis windows with multiply scattered phases (Mayeda & Malagnini 2010). For the choice of the minimization function, it was found in Edwards *et al*. (2008) and Edwards & Rietbrock (2009) that the log-space L2 fit significantly reduces the covariance between t^*_{path}, f_c, and the signal moment. The frequency dependence of Q was tested by varying α in eq. (7) between 0.0 and 0.8.

3.1.2 High frequency spectral fit

The second method to estimate t^*_{path} is that used by Anderson & Hough (1984). This is simply to use only the data above the corner frequency of the spectrum, such that the slope of the spectral decay of log acceleration versus frequency follows a straight line with gradient

$$g = -\pi t^*_{\text{path}}, \tag{10}$$

in the case of frequency independent Q. Events with $M \geq 3.5$ were chosen and frequencies between 10 and 45 Hz were fit such that we are always well above the spectral source corner frequency: the corner frequency of an $M = 3.5$ event with stress drop of 10 MPa [shown by Bay *et al*. (2003, 2005) to be very high for recorded Swiss events] is around 10 Hz (Eshelby 1957; Brune 1970,1971), lower stress drops or larger magnitude events produce even lower source corner frequencies. We can therefore be confident that the data being fit are always uncontaminated by source effects, at least assuming that the Brune (1970) model is correct. In this sense the results are not subject to potential bias effects that may affect simultaneous fit method due to covariance of model parameters. However, on the other hand, the quantity of data is significantly limited by the use of what are, for Switzerland, relatively large earthquakes.

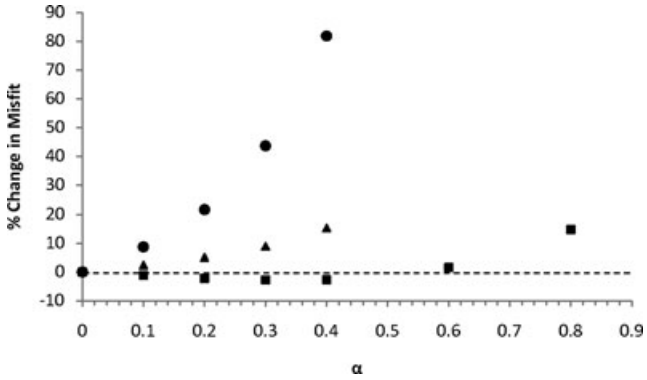

Figure 4. Change in the total misfit of all spectra due to the use of different $Q(f)$ functions. Squares: change in spectral shape misfit. Circles: subsequent change in the misfit of *Cij* to a $1/r$ (first 150 km) and $1/r^{0.5}$ (after 150 km) geometrical spreading model. Triangles: change in misfit of to a $1/R^{\lambda}$ geometrical spreading model, where λ is a free parameter and can vary with distance.

3.2 Frequency dependence of Q

The frequency dependence of Q was tested using several different models, with α ranging from 0 (frequency independent) to 0.8 (strongly frequency dependent). Initial analysis of the misfit of spectra to the model given in eq. (5) showed that the use of $\alpha = 0.3$ resulted in a 2.8 per cent reduction in the misfit over the ensemble of recordings (Fig. 4). Introducing a further degree of freedom into the model may, however, be unjustified and may also lead to higher variance of the other model parameters. We are also interested in the further modelling of the frequency-independent component of the spectrum, C_{ij}, so the variance of this parameter due to modelling uncertainty also needs to be limited. Analysis of the misfit of C_{ij} resulting from the different assumptions of frequency dependent Q ($\alpha = 0.0$–0.4), to an exponential decay function, where

$$\begin{aligned}\log(C_{ij}) = \; & \log(D_i) + \log(A_j) - \min[\lambda_1 \log(r), \lambda_1 \log(r_1)] \\ & - \max\left[\lambda_2 \log\left(\frac{r}{r_1}\right), 0\right], \lambda_1 > 0, \lambda_2 > 0,\end{aligned} \tag{11}$$

was therefore carried out. D_i is a magnitude-dependent term, A_j a site term and λ_1 the rate of decay with distance before the reference hypocentral distance r_1 and λ_2 the rate of decay after r_1. This functional form is later explored in more detail. However, preliminary analysis was undertaken using the best recorded events (greater than 25 stations and with a circular standard deviation of azimuths, $\sigma_{\text{azi}} > 30^{\circ}$: almost 5000 records) to define the appropriate frequency dependence of Q at this stage. The first test was to allow D_i and A_j to vary and fix the rate of decay to that of an expanding spherical wave front in the first 150 km ($\lambda_1 = 1$, $r_1 = 150$ km), followed by an expanding cylindrical wave front ($\lambda_2 = 0.5$). The misfit of C_{ij} to this decay function is shown in Fig. 4. A significant increase in the misfit is introduced for increasing frequency dependence of Q, such that for the value $\alpha = 0.3$, the misfit increased by over

40 per cent. It could be argued, however, that the decay rate may deviate from the simple model assumed and we predefine the result by enforcing a specific rate of decay. Therefore a second test was performed, freeing the λ_1 and λ_2 parameters. It was found that a strong covariance between α and λ is exhibited: increasing α leads to a lower λ (for $\alpha = 0$, $\lambda_1 = 0.82$; while for $\alpha = 0.3$, $\lambda_1 = 0.32$). This then leads to a less dramatic, but nevertheless still significant, increase of the misfit with increasing frequency dependence: around 9 per cent for $\alpha = 0.3$. Essentially we find that although frequency dependent Q can improve the spectral fit, it comes at a cost of a significant increase in the variance of the frequency independent spectral amplitude (C_{ij}). Our findings of frequency independent Q are consistent with those of Morozov *et al*. (2008) who showed that the frequency dependence of Q from numerical simulations gave spurious results of $\alpha \approx 0.5$ when a frequency-independent Q model was used in synthetic simulations. They concluded that it was better to use frequency-independent Q along with geometrical decay that was not fixed based purely on geometrical assumptions such as spherical or cylindrical expansion of the wave front.

4 FITTING Q_0 AND κ MODELS

Typically the whole-path $t^*_{\rm path}$ parameter in eq. (2) is simplified by assuming what is effectively a layer over half-space model, such that

$$t^*_{\rm path} = \frac{r_{ij}}{Q_0 \beta_0} + \kappa_j, \tag{12}$$

where Q_0 and β_0 are the average or reference crustal values of $Q(x,y,z)$ and $\beta(x,y,z)$ respectively, i and j refer to the ith source and jth site and κ_j is synonymous to t^* but specific to the uppermost crustal layer, and is dependent on the recording site (Hanks 1982; Anderson & Hough 1984). As the weathered upper layers of rock and soil are significantly more attenuating than the lithospheric crust, this can account for a great deal of the depth dependence of Q. This parametrization is particularly useful for correcting ground-motion prediction equations (GMPEs) derived from data external to a target region. The so-called host-to-target adjustment can be applied using Q_0 and an average κ value (e.g. Cotton *et al*. 2006) which parametrizes an empirical GMPE in terms of source, site and propagation parameters typically used in stochastic modelling (e.g. Scherbaum *et al*. 2006). Correction of the GMPE can then be made by comparing the derived parameters with regionally derived source-, path- and site-attenuation parameters.

4.1 Separation of κ and Q_0 from $t^*_{\rm path}$

Attenuation measures, $t^*_{\rm path}$, are plotted against distance in Fig. 5. The expected trend of increasing $t^*_{\rm path}$ with distance can be seen. From Fig. 5 it is apparent that, on average, a straight line fit of the r versus $t^*_{\rm path}$ data is sufficient in the first 250 km, although there is a large scatter of individual points. This tells us that a homogeneous Q_0 model is, on average, over numerous source depths, sufficient to explain observations of ground motion up to this distance. Although there are limited data to interpret, above 250 km the homogeneous Q model seems invalid as the degree of attenuation ceases to increase at the same rate.

4.1.1 Iterative linear fit: κ (M1)

The first method used to separate the station values κ_j from the $t^*_{\rm path}$ data is as follows: as κ_j is constant for a particular station, j, we can plot $t^*_{\rm path}$ against hypocentral distance, r, for that station and fit a straight line through the data in the lin-lin space. The gradient of the line is given by $(Q_0\beta_0)^{-1}$ and the intercept of the line is equal to κ_j. The solution robustness is increased through *a priori* knowledge of Q_0: we can then fix the gradient of the best-fit line and only search for the intercept. One way to achieve this is to find a combined Q_0 and average κ value, by using all stations at once. Q_0 can be extracted from the gradient of the best-fit line and then subsequent iterations can be used with station common $t^*_{\rm path}$ data while fixing Q_0.

Using a bootstrap resampling procedure, eq. (12) was fit to $t^*_{\rm path}$ data for all stations. Data were randomly selected with replacement (repetition) from the full data set (excluding strong-motion station recordings). To prevent any bias due to non-uniform distance sampling (fewer recordings at very short and great distances) the data were then sorted by hypocentral distance and binned into 100 equally populated groups. Eq. (12) was fit to the data using an L_2 minimization (the error in $t^*_{\rm path}$ is assumed to be dominant). Only data from distances up to 250 km were used as beyond this distance the model may be inappropriate (Fig. 5). In effect, the greatest distance bin used was centred at about 220 km. The bootstrap procedure was repeated 1000 times to provide mean parameter values and confidence limits of the average values. β_0 was assumed to be 3.5 km s^{-1}, and the resulting Q_0 is denoted $Q_{0,3.5}$.

The resulting model was

$$t^*_{\rm path} = \frac{r}{3.5\,(10^{(3.085\pm0.0502)})} + 0.0157 \pm 0.0026 \text{ s}. \tag{13}$$

Such that $\log_{10}(Q_{0,3.5}) = \log_{10}(1216)\pm0.0502$ (at one standard deviation) which gives a mean $Q_{0,3.5} = 1216$ and upper and lower bounds of 1083 and 1365; and $\kappa_{\rm rec} = 0.0157\pm0.0026$ s (at one standard deviation), where $\kappa_{\rm rec}$ is based on the average of all recordings (and may therefore be influenced by the number of recordings at each station). This analysis shows that the derived $Q_{0,3.5}$ is robust and valid for recordings within around 220 km of the source. For distances above 220 km the derived $Q_{0,3.5}$ will be too low, and therefore attenuation too strong.

To assess our data set for problems such as unresolved $t^*_{\rm path}$ values when f_c lies outside the available frequency bandwidth, we also repeated the inversion on a refined, high confidence data set. This refined data set was obtained by following the method of Viegas *et al*. (2010): that is, for each record we computed the range of possible $t^*_{\rm path}$ values within a tolerance of 5 per cent of the minimum misfit. We removed those t^* values that did not show a clear minimum within this 5 per cent tolerance range. The downside to this is that it clearly results in a reduced data set (in this case we had 24 per cent fewer values), hence may lead to less robust results. The resulting value of Q_0 was 1307. This is a small difference to the value of 1216 found with the full data set, considering the range of values encompassed by the standard deviation.

Examples of best fitting κ_j values from the iterative linear fit method are shown in Fig. 6. The $\kappa_{\rm rec}$ value is higher than that found by Bay *et al*. (2003, 2005), who found an average value of $\kappa = 0.0125$ s. At 25 Hz this equates to a difference of 25 per cent in the predicted amplitude spectrum. This could be attributed to different stations being used to form the average κ (the Bay *et al*. 2003 study used data from the old short-period network). For instance, they state that only sensors on the National Earthquake Hazards Reduction Program (NEHRP) (BSSC 2003) class A or B rock conditions are used. In addition it is possible that a higher proportion of recordings are made on sensors with higher κ in this report with respect to the Bay *et al*. (2003) study. Furthermore, the data used by Bay *et al*. (2003) were recorded mostly on short-period

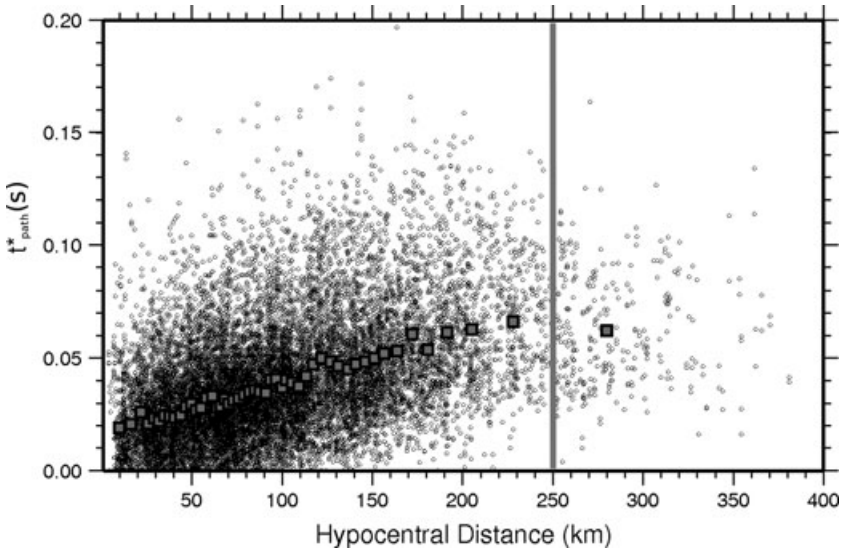

Figure 5. Plot of t^* (path attenuation) against hypocentral distance. Squares are the average t^*path values for binned distances and magnitudes where each bin has the same number of t^*path values. The grey line indicates the 250 km point beyond which, data were not used to derive Q_0.

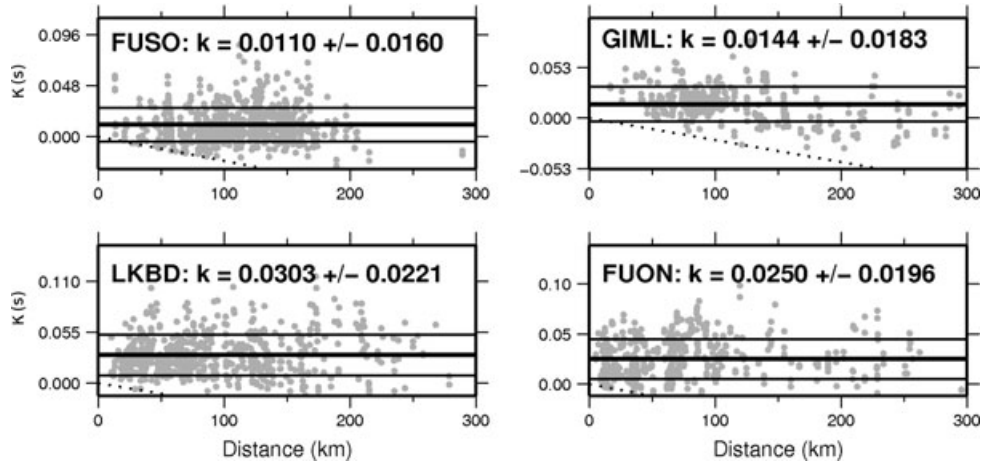

Figure 6. Determination of κ using the iterative linear method (M1). K is plotted against distance for selected stations of SDSNet: FUSIO (labelled FUSO); GIMEL (labelled GIML); LKBD and FUORN (labelled FUON). The heavy solid line indicates the mean, and the light solid line the standard deviation of the computed κ value. The dotted line indicates the minimum possible κ at a particular distance (due to the restriction that $t^*_{\rm path} > 0$ s). Note that data were not used to compute κ beyond distances of 250 km.

instrumentation which were band limited to 12 Hz. The uncertainty of their κ parameter would therefore be much higher than for this study for which frequencies up to 30 Hz are fit.

4.1.2 Matrix inversion fit: $\kappa(M_2)$

If the distribution of recording distance and station numbers is non-uniform, the κ_j values can influence the estimated Q_0. For instance, if only stations on low-velocity rock are included at very short distances, and these stations tend to have particularly high κ_j values, the apparent crustal attenuation would seem lower, and as such Q_0 would increase. The second method simultaneously solves for Q_0 and κ_j values to decouple some of the trade-offs. Eq. (12) can be represented by the form

$$d = G\mathrm{m}, \tag{14}$$

which can be expanded to

$$\mathbf{d} = \begin{bmatrix} r_{11} & 1 & 0 & \cdots & 0 \\ r_{21} & 1 & 0 & \cdots & 0 \\ r_{12} & 0 & 1 & \cdots & 0 \\ \vdots & \vdots & \vdots & \cdots & \vdots \\ r_{MN} & 0 & 0 & \cdots & 1 \end{bmatrix} \begin{bmatrix} (Q_0\beta)^{-1} \\ \kappa_1 \\ \kappa_2 \\ \vdots \\ \kappa_N \end{bmatrix}, \tag{15}$$

and solved to find the best-fitting model parameters in terms of the least-squared residual. Assuming that the $t^*_{\rm path}$ estimates are normally distributed around the true value and that the mean and standard deviation of the estimates are independent of the station, the covariance of the model parameter matrix **m** can be computed.

$$C_m = \sigma^2_{t^*_{\rm path}} (G^T G)^{-1}, \tag{16}$$

where $\sigma_{t^*_{\rm path}}$ is the standard deviation of the $t^*_{\rm path}$ estimates. This gives a value representative of the confidence of the mean value for a particular model parameter. In addition to this confidence value,

the standard deviation of measured κ can be found by comparing the mean and record specific κ_j values. Using the simultaneous matrix inversion for $Q_{0,3.5}$ and κ_j we find a mean $Q_{0,3.5} = 1194$, which leads to a negligible difference in the amplitude spectrum with respect to the value of 1216 found above. In this case the average κ is defined by:

$$\kappa_{\text{stns}} = \frac{1}{N}\sum_{j=0}^{N}\kappa_j, \tag{17}$$

where j indicates a particular site and N is the number of sites. κ_{stns} is therefore the average κ of all stations (including strong-motion sensors) used in the database (regardless of the number of recordings used from that station). This leads to a κ_{stns} of 0.020 s. This is higher than the κ_{rec} derived earlier (0. 0157 s: from eq. 13). The explanation for this is the different definition of the mean: the number of recordings at each station also influences κ_{rec}.

The station κ_j values from both methods (M1: iterative linear fit method; M2: simultaneous matrix method) are given in Table 2. There are negligible differences between the values derived from the two methods. It should be noted, however, that despite the negligible differences between the methods, the derivation of κ is very uncertain (note for instance the standard deviations in Table 2). This uncertainty may be due to a combination of a simplified model or other factors such as data or modelling bias. κ_j values from method M2 are plotted by location in Fig. 7. Stations exhibiting very low attenuation may show negative values of κ_j. This is a combination of the limitation of the resolution of the method and potentially the effect of site-specific amplification or resonance features being reflected in κ_j. In reality a minimum value, $\kappa_{\text{min}} = 0$ s can be imposed, assuming that path attenuation is fully described by the crustal Q_0. However, in this case the site amplification term should be carefully considered.

5 t^*_{path} FROM THE FITTING METHOD OF ANDERSON & HOUGH (1984)

The κ value essentially defines a low-pass filter of displacement amplitude. It is independent of magnitude and path distance. Therefore it is difficult to distinguish from the corner frequency of the earthquake source model (Boore *et al*. 1992). It can be argued that simultaneous fit method used to obtain t^*_{path} thus far can be sensitive to the trade-off between source and site. To check the values defined using the simultaneous fit method, we therefore re-estimate t^*_{path} using a method that is insensitive to this trade-off. Assuming that an $M_{\text{W}} = 3.5$ event has a 10 MPa stress drop [which is high for Switzerland (Bay *et al*. 2003)], the source corner frequency is 6.1Hz (Eshelby 1957; Brune 1970, 1971). For a constant stress drop, increasing M_{W}, leads to a decrease in the source corner frequency. Therefore we can say that for $M_{\text{W}} \geq 3.5$, data with $f > 10$ Hz are above the corner frequency. Anderson & Hough (1984) showed that for frequency-independent Q_0, the slope of the log Fourier acceleration spectrum above the corner frequency is given by eq. (10). t^*_{path} were computed for 823 horizontal records (where each horizontal component is one record) of 48 events.

Using the newly computed t^*_{path}, $Q_{0,3.5} = 1200$ was used to find κ_j by solving eq. (12). $Q_{0,3.5} = 1200$ was used as the quantity of data remaining were too few to robustly define $Q_{0,3.5}$ in addition to κ_j. Fig. 8 shows a comparison of the κ_j values derived from the simultaneous fit method and the t^*_{path} method of Anderson & Hough (1984). The κ_j values computed following this method are consistent with those computed using the simultaneous fit method, following a 1:1 trend, albeit with very large scatter and some outliers. The limited data availability when using only $M > 3.5$ meant that not all stations could be compared. As the values are generally consistent (within the errors of the methods), it can be concluded that the simultaneous fit method did not introduce systematic bias or trade-off. The significantly higher quantity of data available to the simultaneous fit method means that the values presented in Table 2 are more robust and reliable.

6 COMPARISON OF κ AND OTHER SITE TERMS ($V_{\text{s}}30$, AMPLIFICATION)

$V_{\text{s}}30$ is the average shear wave velocity in the upper 30 m of the rock and/or soil. As materials with lower shear wave velocity tend to have more pore space in which fluids and gases reside, there may be a correlation with κ, which is sensitive to material properties. For several stations of the SDSNet, detailed site characterization has been undertaken (Fäh & Huggenberger 2006; Havenith *et al*. 2007; Fäh *et al*. 2009). This included the derivation of shear wave velocity profiles using techniques such as multi-channel analysis of surface waves (MASW) and array measurements of ambient noise (e.g. Fäh *et al*. 2008; Poggi & Fäh 2010). From the resulting velocity profiles $V_{\text{s}}30$ was obtained. Fig. 9 shows a loose correlation ($R^2 = 0.381$) between $V_{\text{s}}30$ and $\log(\kappa)$. The relation is given by

$$\log(\kappa) = -2.78 \times 10^{-04}(V_{\text{s}}30) - 1.49. \tag{18}$$

Or alternatively, if comparing $V_{\text{s}}30$ and κ

$$\kappa = -8.38 \times 10^{-06}(V_{\text{s}}30) + 0.0289. \tag{19}$$

Using the $\log(\kappa)$ fit, the κ value equivalent to a $V_{\text{s}}30 = 1100$ m s^{-1} [which is approximately equivalent to the reference rock model used (Poggi *et al.* 2011)] is 0.016 s. However, it is difficult to distinguish which fit is better [log (κ) or κ vs. $V_{\text{s}}30$] due to the large scatter of values. Unfortunately relatively few data points were available due to the lack of $V_{\text{s}}30$ measurements. Values of $V_{\text{s}}30$ and κ from Drouet *et al*. (2010) along with the $V_{\text{s}}30$-κ relations of Silva *et al*. (1998) and Chandler *et al*. (2006) are also included in Fig. 9. There is considerable scatter, but on average the values of Drouet *et al*. (2010), consisting of locations in the French Alps, are consistent with the values measured in Switzerland. The $V_{\text{s}}30$ measurement for the data of Drouet *et al*. (2010) was much more uncertain than that of the $V_{\text{s}}30$ for the Swiss sites, which causes a great deal of the scatter. The relationships of Silva *et al*. (1998) and Chandler *et al*. (2006) tend to give higher κ for specific $V_{\text{s}}30$ values. The Silva *et al*. (1998) relationship was developed for North America and the Chandler *et al*. (2006) relationship was derived from a number of sources worldwide. The difference may therefore lie with the methodology and model used (both for $V_{\text{s}}30$ and κ) rather than regional variation. Fig. 10 also shows a loose correlation ($R^2 = 0.345$) between the logarithm of the observed frequency independent amplification (A_j) relative to the average rock condition for the sites used (see Poggi *et al.* 2010) and $\log(\kappa)$:

$$\log(\kappa) = 0.764\left[\log(A_j)\right] - 1.77. \tag{20}$$

For the null amplification condition ($A_j = 1$), such that the V_{s} profile is the reference rock, $\kappa = 0.017$ s. Note therefore, how the relations of κ, amplification and $V_{\text{s}}30$ are consistent: for $A_j = 1$ and for $V_{\text{s}}30 = 1100$ m s^{-1}, both characteristics of the reference rock model, $\kappa \approx 0.016$ s. The relation with amplification suggests that sites with shear wave velocity profiles lower than the reference exhibit higher κ. The interrelation between amplification, κ and $V_{\text{s}}30$

Table 2. Station κ values from both the iterative linear fit (M1) and matrix (M2) methods. The difference in the amplitude spectrum at 25 Hz is indicated as a fraction between the M1 and M2 values.

Station name	κ(M1) (s)	κ(M1) Standard deviation (s)	κ(M2) (s)	κ(M2) Standard error (s)	# Rec	κ(M2)–κ(M1) (s)	Ratio κ(M2)/ κ(M1) (at 25 Hz)
ABSI	0.0541	0.0266	0.0531	0.0028	40	−0.0009	1.0764
ACB	0.0261	0.0169	0.0259	0.0014	184	−0.0002	1.0156
AIGLE	0.0139	0.0157	0.0142	0.0008	537	0.0004	0.9728
BALST	0.0028	0.0146	0.0023	0.0008	557	−0.0004	1.0346
BERNI	0.0117	0.0171	0.0114	0.0007	619	−0.0004	1.0285
BFO	0.0012	0.0171	−0.0002	0.0046	15	−0.0014	1.1121
BNALP	0.015	0.0195	0.0142	0.0007	818	−0.0009	1.0693
BOURR	0.0285	0.021	0.0288	0.0007	665	0.0002	0.9818
BRANT	0.0041	0.0221	0.0033	0.0011	280	−0.0007	1.0592
CHDAV	0.0192	0.0177	0.0186	0.0024	54	−0.0006	1.0466
CHDAW	0.0346	0.0201	0.0339	0.0018	99	−0.0007	1.0605
CHIR2	0.0158	0.0127	0.015	0.0015	139	−0.0008	1.0609
CHKAM	0.0161	0.0187	0.0159	0.002	81	−0.0002	1.0174
CHMEL	0.0085	0.013	0.0076	0.0031	33	−0.0009	1.0697
CHSTR	0.0195	0.0109	0.0189	0.0057	10	−0.0006	1.0504
DAVA	0.05	0.0274	0.0496	0.0015	144	−0.0004	1.0355
DAVON	0.0469	0.0193	0.0462	0.0014	174	−0.0006	1.0522
DAVOX	0.027	0.0174	0.0267	0.001	379	−0.0003	1.0259
DIX	0.0051	0.0157	0.0046	0.0008	529	−0.0005	1.0369
DOETR	0.0185	0.0178	0.0177	0.0014	161	−0.0008	1.0611
DOI	0.0188	0.0278	0.0313	0.0052	16	0.0125	0.3753
EMV	−0.0025	0.0126	−0.003	0.0008	491	−0.0005	1.039
FLACH	0.025	0.0139	0.0242	0.0013	182	−0.0008	1.0635
FUORN	0.025	0.0196	0.0245	0.0008	521	−0.0005	1.0384
FUSIO	0.011	0.016	0.0101	0.0007	791	−0.0009	1.0741
GIMEL	0.0144	0.0183	0.0148	0.0009	429	0.0004	0.9698
GRYON	0.0082	0.0148	0.0081	0.0011	273	−0.0001	1.006
GUT	−0.0092	0.015	−0.0103	0.0033	30	−0.0011	1.0922
HASLI	0.0085	0.0205	0.0077	0.0008	619	−0.0008	1.0684
KAMOR	0.0135	0.0212	0.0129	0.0013	201	−0.0006	1.0507
KIZ	−0.0068	0.0152	−0.008	0.0029	39	−0.0012	1.0989
KOSI	0.0484	0.0221	0.0474	0.0037	24	−0.001	1.081
LIENZ	0.0133	0.0177	0.0125	0.0011	253	−0.0008	1.064
LKBD	0.0303	0.0221	0.0294	0.0008	585	−0.0008	1.0686
LLS	0.0033	0.0191	0.0025	0.0008	640	−0.0008	1.065
LSD	−0.006	0.0106	−0.0068	0.0038	22	−0.0008	1.0618
MABI	−0.0006	0.0146	−0.0009	0.0021	75	−0.0003	1.0251
MDI	0.0153	0.0215	0.0153	0.0022	68	0.0000	1.0007
MELS	0.0073	0.0142	0.0065	0.0015	147	−0.0008	1.063
MMK	0.0025	0.0137	0.0018	0.0008	611	−0.0007	1.0576
MONC	0.0388	0.0231	0.0427	0.0048	16	0.0039	0.7349
MOSI	0.0811	0.0342	0.0805	0.0021	74	−0.0005	1.0425
MRGE	−0.0079	0.0082	−0.0083	0.0025	55	−0.0004	1.0342
MUGIO	−0.0058	0.019	−0.0059	0.001	361	−0.0001	1.0062
MUO	0.0541	0.0225	0.0533	0.0009	443	−0.0008	1.0608
NARA	0.0223	0.0177	0.0216	0.002	84	−0.0007	1.06
OTTER	0.0184	0.0084	0.0184	0.0038	22	−0.0001	1.0046
PIORA	−0.0036	0.0122	−0.0044	0.0035	26	−0.0007	1.0588
PLONS	0.0069	0.0197	0.0064	0.001	373	−0.0005	1.0378
RITOM	0.0092	0.0162	0.0085	0.0017	115	−0.0007	1.0591
ROSI	0.0514	0.0202	0.0504	0.0034	27	−0.001	1.0811
RSP	0.0059	0.0163	0.0081	0.0034	30	0.0022	0.8382
SALAN	0.0037	0.0141	0.0036	0.001	359	−0.0001	1.0094
SALO	0.0472	0.0266	0.0464	0.0045	16	−0.0008	1.0636
SAUR	0.0163	0.006	0.0162	0.0031	33	−0.0002	1.0134
SBAF	0.0219	0.0105	0.0218	0.0036	24	0.0000	1.0036
SBAP	0.0186	0.0098	0.0185	0.0036	25	−0.0001	1.0079
SBAT	0.0223	0.0097	0.0221	0.0031	33	−0.0001	1.0113
SBIS	0.0301	0.0045	0.0301	0.0032	32	−0.0001	1.0054
SCUC	0.028	0.0137	0.0276	0.0024	57	−0.0003	1.0266
SENIN	0.0179	0.0171	0.0173	0.0008	542	−0.0005	1.0441
SIOO	0.0369	0.0116	0.0366	0.0046	15	−0.0002	1.0162

Table 2. *Continued*

Station name	κ(M1) (s)	κ(M1) Standard deviation (s)	κ(M2) (s)	κ(M2) Standard error (s)	# Rec	κ(M2)–κ(M1) (s)	Ratio κ(M2)/ κ(M1) (at 25 Hz)
SIOV	0.0165	0.0139	0.0162	0.003	35	−0.0003	1.0219
SKAF	0.0024	0.0063	0.0022	0.0029	37	−0.0002	1.0188
SLE	0.0065	0.0184	0.006	0.0009	524	−0.0005	1.0391
SMUR	0.0184	0.0149	0.0181	0.0032	31	−0.0003	1.0218
SMZW	0.0212	0.0113	0.0211	0.0033	30	−0.0001	1.0056
SRHB	0.0293	0.0087	0.0292	0.0033	29	0.0000	1.0038
STEIN	0.0195	0.0179	0.0193	0.0015	144	−0.0002	1.0194
STSP	0.0395	0.0148	0.0392	0.0031	33	−0.0003	1.0223
SULZ	0.0142	0.0191	0.0136	0.0008	630	−0.0006	1.0443
SZER	0.0201	0.0117	0.0198	0.0026	47	−0.0003	1.0203
TONGO	0.0109	0.0144	0.0101	0.0028	41	−0.0008	1.0621
TORNY	0.0215	0.0202	0.0216	0.0009	422	0.0001	0.9948
TRULL	0.0173	0.0127	0.0165	0.0015	148	−0.0007	1.0591
TUE	0.0165	0.0164	0.0158	0.0028	42	−0.0007	1.0552
UBR	0.0498	0.0369	0.0482	0.0048	15	−0.0016	1.1329
VDL	0.0088	0.0172	0.0081	0.0007	689	−0.0007	1.0554
WEIN	0.0254	0.0205	0.0246	0.0014	176	−0.0008	1.0625
WILA	0.0424	0.0209	0.0416	0.0009	481	−0.0009	1.0705
WIMIS	0.0108	0.0182	0.0102	0.001	375	−0.0006	1.0494
WTTA	0.0483	0.0269	0.0499	0.0032	33	0.0017	0.8775
ZUR	0.0215	0.0167	0.0206	0.0009	449	−0.0009	1.0713

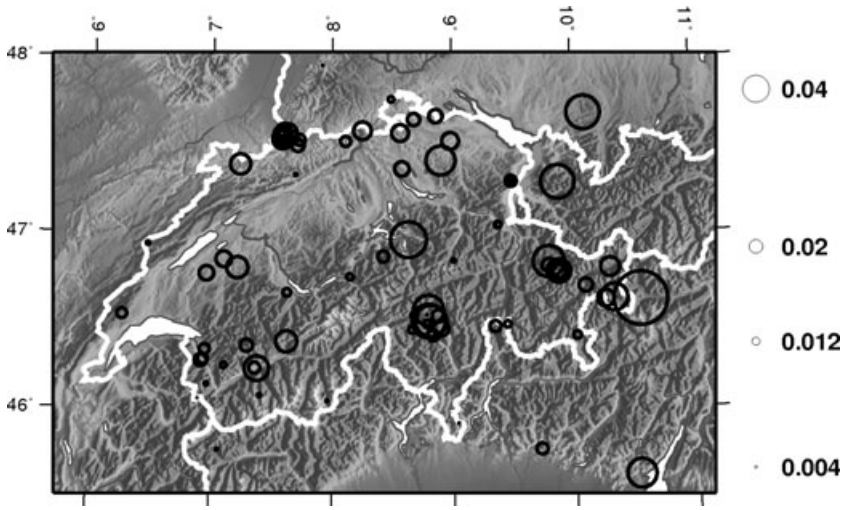

Figure 7. Station κ from the matrix inversion (M2) plotted against topography for the Q_0 model.

may be due to material properties of the rock, or due to phenomena such as weathering, unconsolidated material or the presence of fluids in the pores of the rock. Such a relation is logical, as for sites in sedimentary basins with lower shear wave velocities (e.g. in the Swiss Foreland) both the attenuation due to pore-fluid inclusion and the site amplification are expected to be higher.

7 κ SUMMARY

κ values have been computed for the stations of the SDSNet. The average crustal attenuation can be described by a quality factor of $Q_{0,3.5} = 1216$ when assuming an average crustal velocity of 3.5 km s^{-1}. The mean κ value is found to be $\kappa = 0.016$ s which equates to a Q of around 30 or a damping ratio ($1/2Q$) of 0.016 if attributed to a layer of 1 km in thickness with an average V_s of 2 km s^{-1}. The highest κ values tend to occur at stations with low V_s30. Depending on the method applied we obtain slightly different κ values, however, the differences are much smaller than the measurement errors. It is proposed that station κ values are taken from the matrix inversion [κ(M2) in Table 2], as this method should be least affected by data distribution inconsistencies (e.g. strong motion instrumentation only recording at short distances from earthquakes). The error value given for κ(M2) in Table 2 is the standard error of the mean and does not fully reflect the standard deviation of measured κ values. To include the observed scatter in κ, which may be due to, for example, propagation direction, the standard deviation given for κ(M1) can be used. For the κ value consistent with the reference site of Poggi *et al*. (2011), $V_s30 \approx 1100$ m s^{-1} it is recommended that eq. (18) is used, which leads to $\kappa(V_s30 = 1100 \text{ m s}^{-1}) = 0.016$ s for a corresponding $Q_{0,3.5} = 1216$. κ values in the Basel area are typically high. This is expected, as the region is characterized by sedimentary rocks in the upper layers. The highest κ value for which a detailed site characterization report is available is MUO ($\kappa = 0.053$ s). This station is on a mountain peak, with V_s30 of around 1000 m s^{-1}. This is not characteristic of where we would expect a high κ value. However, the high κ may be due to

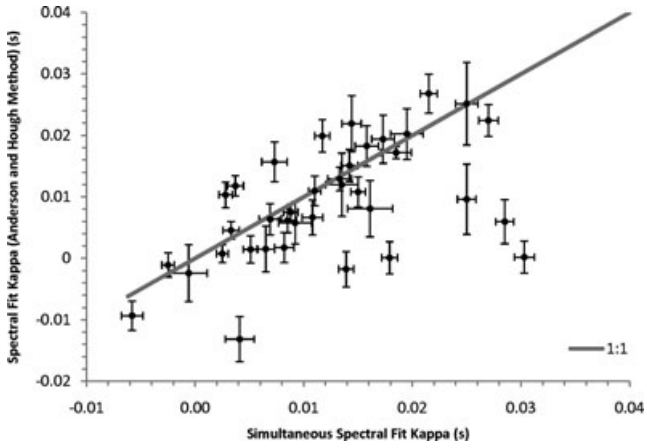

Figure 8. Comparison of κ derived using the simultaneous fit method presented earlier and the method of Anderson & Hough (1984) where only events with $M \geq 3.5$ and frequencies between 10 and 45 Hz are fit. Error bars indicate the standard error.

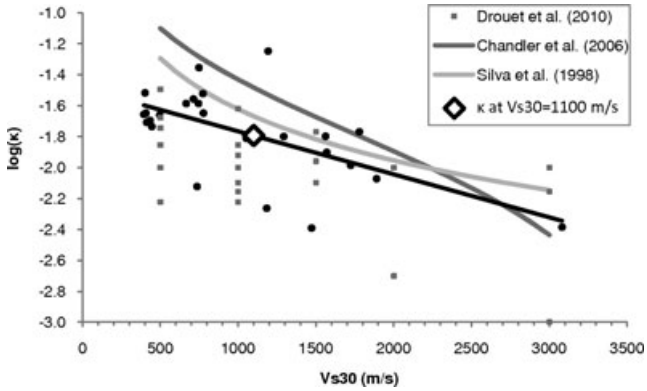

Figure 9. log(κ) plotted against V_s30 for sites with available (measured) V_s30 values of the SDSNet (circles) and from Drouet *et al*. (2010) (squares). The best fit of the SDSNet data (eq. 18) is shown by the solid black line. The relations of Silva *et al*. (1998) and Chandler *et al*. (2006) are plotted for comparison. At $V_s30 = 1100$ m s^{-1}, $\kappa = 0.016$ s.

topographic effects. For station WILA, located at the foot of a hill, the derived V_s30 measurement is around 600–700 m s^{-1}. This station showed $\kappa = 0.042$ s. One caveat of this analysis is that Q may be dependent on depth due to changes in material properties such as density. This, coupled with the covariance between epicentral recording distance and penetration depth, may lead to the underestimation of attenuation at short epicentral distances, and overestimation of attenuation at longer epicentral distances when using the Q_0 and κ model approximation of eq. (2).

8 LAYERED Q MODEL

A refinement of the Q_0 and κ model is now presented: the development of a representative Q profile with depth (z). A tomographic approach to the problem is used to solve eq. (2) (e.g. Rietbrock 2001; Eberhart-Philipps *et al*. 2008; Edwards *et al*. 2008; Edwards & Rietbrock 2009). To verify that the $t^*_{\rm path}$ values measured using the windows defined by the duration of shaking are appropriate for tomographic modelling, they are first compared with values computed using 2.56 s windows directly after the first S-phase arrival (Fig. 11). This showed no discernible trend in the $t^*_{\rm path}$ values with distances up to over 200 km, although the value measured from the

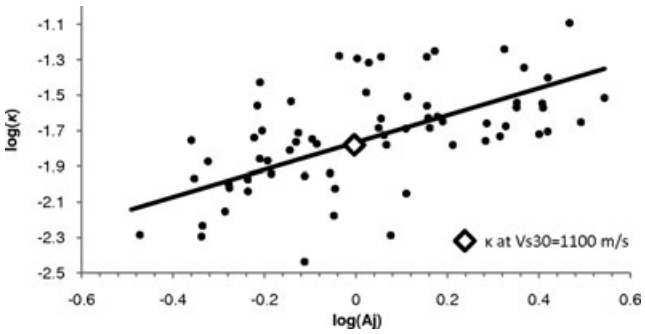

Figure 10. log(κ) plotted against the frequency-independent amplification (Poggi *et al.* 2011) relative to the average Swiss rock condition. At null amplification [i.e. a V_s profile equivalent to the reference rock (Poggi *et al.* 2011)], which is equivalent to $V_s30 \approx 1100$ m s^{-1}, $\kappa = 0.016$ s.

2.56 s window is consistently higher by, on average, 24 per cent (Fig. 11). The reference velocity model, $\beta(z)_{\rm genericrock}$, is taken from the reference rock profile in Poggi *et al.* (2011) (Table 3). Lateral variations in Q are averaged out to give a representative layer value. However, as $t^*_{\rm path}$ depends on both Q and β, variations in β that are not included in the reference model (e.g. lateral variations of velocity) are mapped into Q. As such the $Q(z)_{\rm ref}$ model describes the attenuation properties of the rock, normalized to a common velocity reference: velocities slower than the reference will give rise to higher attenuation, which is in turn reflected in lower $Q(z)_{\rm ref}$ values. The 1-D $Q(z)_{\rm ref}$ model is given by

$$Q(z)_{\rm ref} = \frac{1}{XY}\int_0^X \int_0^Y \left[\frac{Q(x,y,z)\beta(x,y,z)}{\beta(z)_{\rm generic\ rock}}\right] {\rm d}y{\rm d}x, \qquad (21)$$

where x, y and z are the Cartesian coordinates, X and Y are the limits of the model in the x and y directions, respectively. Interpretation of Q in terms of material properties is therefore beyond the scope of this paper: for that purpose a 3-D shear wave velocity model would be required in addition to t^* estimates taken directly from the direct S wave. Instead the focus is on the inclusion of depth information in the attenuation model for the use in forward modelling for hazard applications, such as stochastic simulations.

The 1-D $Q(z)_{\rm ref}$ model is shown in Fig. 12 and Table 3 and shows a clear increase of $Q_{\rm ref}$ with depth up to around 25 km. $Q_{\rm ref}$ then briefly decreases for greater depths. Considering the resolution of the method the differences between the Foreland and Alpine models are small at depths greater than 2 km. In the upper-most layers the Foreland model shows significantly stronger attenuation [lower $Q(z)_{\rm ref}$]. This is expected due to the basin geology found in this region: in this case lower β and lower Q are expected than the references. On the other hand, at depth the Foreland exhibits slightly lower attenuation. Note that due to the non-unique solution of the tomographic model, the average model does not always lie in between the Foreland and Alpine models.

Lateral differences in the attenuation or velocity of the upper layers can be accounted for using a site-specific correction ($\Delta\kappa$).

$$\Delta\kappa_j = \frac{1}{N}\sum_{i=1}^{N}\left(t^*_{\rm path} - \int_{r=0}^{R}\frac{{\rm d}r}{Q(z)_{\rm ref}\beta(z)_{\rm generic\ rock}}\right), \qquad (22)$$

with N the number of records at site j, and other parameters as in eq. (2). Site-specific correction values ($\Delta\kappa$) are computed for the average 1-D Q model (Fig. 13, Table 4). In this case the $\Delta\kappa$ values can be positive or negative as the upper layer of attenuation (usually accommodated by κ) is already included in the 1-D Q model. In general the higher $\Delta\kappa$ values are located in the Foreland: accounting

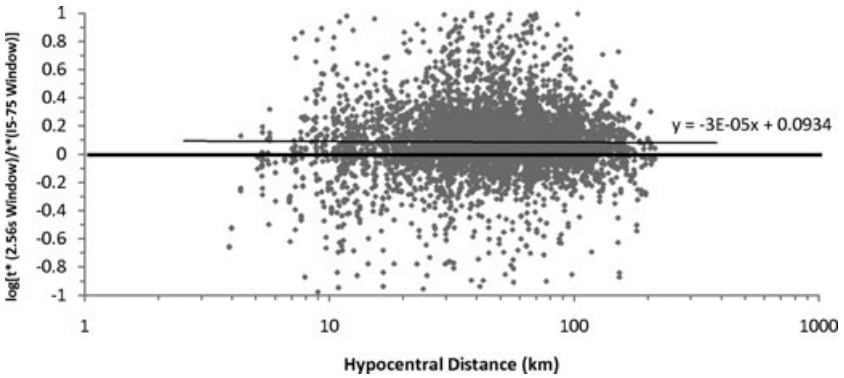

Figure 11. Comparison of measured t^* values using the significant duration of shaking (v5–75) window (as used throughout this study) with those measured from short (2.56 s) windows after the first *S* arrival.

Table 3. Q models. Q values should be linearly interpolated between depths. The percentage difference column is indicative of the difference in attenuation between the Foreland and Alpine $Q_{\rm ref}$ models and assumes a wave travelling through a homogeneous Q_0 at 3.5 km s^{-1} for 50 km.

Depth (km)	$\beta(z)_{\rm genericrock}$ (km s^{-1})	Average $Q(z)_{\rm ref}$	Foreland $Q(z)_{\rm ref}$	Alps $Q(z)_{\rm ref}$	Per cent difference at 50 km
0	1.10	–	–	–	–
1	2.91	255	154	222	8.5
2	3.18	222	170	210	4.9
8	3.49	988	1440	1330	−0.3
13	3.57	904	1790	762	−3.4
22	3.59	2650	3080	1720	−1.2
30	4.69	1500	1750	1170	−1.3
40	4.10	1160	1620	940	−2.0

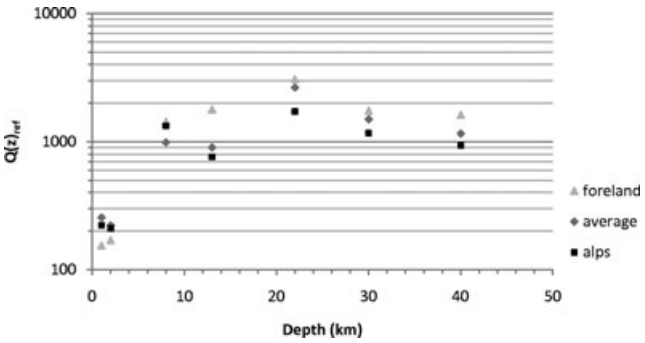

Figure 12. Q as a function of depth. Lin-space linear interpolation between the inversion nodes is assumed.

for the lower Q seen in the Foreland specific Q model. In general the $\Delta\kappa$ values are much lower than the κ values determined using the model of Anderson & Hough (1984) showing that the layered Q model accounts for much of the attenuation that originally was assigned to κ (Fig. 7). The $\Delta\kappa$ value now indicates the deviation of the average 1-D Q model for a particular site.

Fig. 14 shows the relation of $\Delta\kappa$ to measured $V_{\rm s}30$ at a number of sites investigated. This relation can be used to select $\Delta\kappa$ for site-specific simulations. At $V_{\rm s}30 = 1100$ m s^{-1}, consistent with the reference rock model (Poggi *et al.* 2011), $\Delta\kappa = 0.00$ s.

$$\Delta\kappa = -3.11 \times 10^{-2}\log(V_{\rm s}30) + 9.51 \times 10^{-2}. \quad (23)$$

$\Delta\kappa$ in the Basel area are typically high, this is expected, as the region is characterized by sedimentary rocks in the upper layers. As with the κ values, the highest $\Delta\kappa$ value for which a site characterization report is available is MUO ($\Delta\kappa = 0.035$ s). This station is on a mountain peak, with Vs30 of around 1000m/s. This is not characteristic of where we would expect a high $\Delta\kappa$ value. However, the high $\Delta\kappa$ may be due to topographic effects. In this case the $\Delta\kappa$ value for MUO affected the overall fit of eq. (23) significantly, it was therefore removed. WILA showed the next highest $\Delta\kappa = 0.0249$ s for sites with characterization available. This station is located at the foot of a hill, with a derived $V_{\rm s}30$ measurement of around 600–700 m s^{-1}.

To use the tomographic Q model in SMSIM (Boore 2003) the following formula can be used to compute $Q_{0,3.5}$, the homogeneous Q_0 for $\beta = 3.5$ km s^{-1}:

$$Q_{0,3,5} = \frac{\sqrt{D^2 + R_{\rm e}^2}}{3.5(t^* + \Delta\kappa)}, \quad (24)$$

where t^* for the path is obtained from the 1-D Q and velocity model (Table 5), $\Delta\kappa$ depends on the site (Table 4), D is the source depth and $R_{\rm e}$ is the epicentral distance. Note that for sites with very low attenuation (negative $\Delta\kappa$) at near-source distances, this can lead to negative Q. This is, however, simply a limitation of the model as there are little data in this range. For these cases it is suggested that $Q_{0,3.5}$ is set to the average crustal value of 1216.

Finally, It should be reiterated that the model of Anderson & Hough (1984) (Q_0 and κ) and the 1-D layered $Q_{\rm ref}$ model and $\Delta\kappa$ values should be used completely independently. That is, either the layered $Q_{\rm ref}$ and $\Delta\kappa$ values should be used, or the $Q_{0,3.5} = 1216$ and κ values should be used, not a combination of both, as the 1-D layered $Q_{\rm ref}$ model already includes the attenuation usually attributed to Anderson & Hough (1984) κ.

9 COMPARISON OF ATTENUATION MODELS

Two distinct models were presented, one with a depth-dependent Q, and one with a homogeneous Q_0. Comparisons of these models are shown in Fig. 15. Due to the use of κ, which is independent of distance, the Q_0 model also leads to variation of attenuation with depth and distance. However, the depth dependent Q model shows more variation with depth than the Q_0 model. In general, the 1-D $Q_{\rm ref}$ model leads to stronger attenuation for very shallow events, regardless of distance. On the other hand, for deeper events, the 1-D $Q_{\rm ref}$ model leads to lower attenuation regardless of epicentral distance. If we consider that Q is indeed depth dependent throughout the crust, as in the 1-D model, then the Q_0 model will not include the impact of source location on $t^*_{\rm path}$ for epicentral distances beyond 30 km. This is a significant disadvantage, however, due to the scatter of $t^*_{\rm path}$ values used in the model derivation, it is not clear which

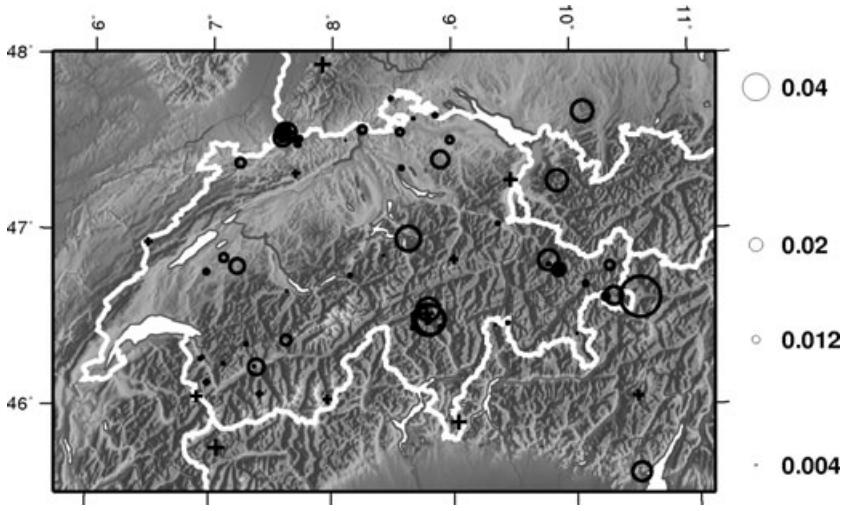

Figure 13. $\Delta\kappa$ values plotted against topography for the average 2-D layered model. Circles indicate positive $\Delta\kappa$ (stronger than average attenuation), crosses indicate negative $\Delta\kappa$ (lower than average attenuation).

Table 4. $\Delta\kappa$ values for the SDSNet stations relative to the average 1-D $Q_{\rm ref}(z)$ model.

Station	$\Delta\kappa$ (s)	Station	$\Delta\kappa$ (s)	Station	$\Delta\kappa$ (s)	Station	$\Delta\kappa$ (s)
ABSI	0.03	DOI	0.0013	MRGE	−0.026	SKAF	−0.0078
ACB	0.0112	EMV	−0.0201	MUGIO	−0.0241	SLE	−0.0106
AIGLE	−0.0012	FLACH	0.0092	MUO	0.035	SMUR	0.0042
BALST	−0.0138	FUORN	0.0073	NARA	0.0019	SMZW	0.0146
BERNI	−0.0064	FUSIO	−0.008	OTTER	0.0132	SRHB	0.0229
BNALP	−0.0034	GIMEL	−0.0022	PIORA	−0.0238	STEIN	0.0033
BOB	0.0243	GRYON	−0.0082	PLONS	−0.0093	STSP	0.0231
BOSI	0.0067	HASLI	−0.0096	RISI	0.0059	SULZ	−0.002
BOURR	0.0126	KAMOR	−0.0022	RITOM	−0.0116	SZER	0.0048
BRANT	−0.0133	KIZ	−0.0248	ROSI	0.0243	TONGO	−0.0098
CHDAV	0.0037	KOSI	0.0232	RSP	−0.0132	TORNY	0.0048
CHDAW	0.0158	LIENZ	−0.0045	SALAN	−0.0139	TRULL	0.0015
CHIR2	−0.0042	LKBD	0.0123	SALO	0.0248	TUE	−0.0064
CHKA2	−0.0226	LLS	−0.0154	SAUR	0.0061	VDL	−0.0102
CHKAM	0.0011	LSD	−0.027	SBAF	0.0171	WEIN	0.0089
CHMEL	−0.0052	MABI	−0.0209	SBAP	0.013	WILA	0.0249
CHSTR	−0.0011	MDI	−0.0012	SBAT	0.0152	WIMIS	−0.0053
DAVA	0.031	MELS	−0.0085	SBIS	0.0235	WTTA	0.033
DAVON	0.0278	MFSFA	−0.0121	SCUC	0.0109	ZUR	0.0045
DAVOX	0.01	MMK	−0.0161	SENIN	0.0001	–	–
DIX	−0.0137	MONC	0.0255	SIOO	0.0261	–	–
DOETR	−0.0013	MOSI	0.0561	SIOV	0.0014	–	–

model is better, or indeed if the additional complexity in the 1-D model is statistically justified.

In comparison of other $Q(f)$ models from the Alpine and Swiss region (Fig. 16), the $Q_{0,3.5} = 1216$ is consistent with Douglas *et al*. (2010), who analysed data for France, mainly events in the Alps, Rhine Graben and the Pyrenees. The model is also similar to the model proposed by Drouet *et al*. (2010) for the Rhine Graben, although they also found frequency-dependent Q. Other models for the Alpine region tend to find lower Q, with quite strong frequency dependence (Drouet *et al*. 2010 Alpine model; Bay *et al*. 2003; Morasca *et al*. 2006).

10 APPARENT GEOMETRICAL DECAY

The attenuation of energy independent of frequency is now explored after accounting for the attenuation using the frequency-independent layered $Q(z)_{\rm ref}$ model. This describes the change of the signal moment ($\hat{\Omega}_{ij}$) with distance, where

$$\hat{\Omega}_{ij} = \frac{C_{ij}}{2\pi} = \frac{M_0 F \theta_{\lambda\phi}}{4\pi r_0 \rho v^3} S(r), \tag{25}$$

(Brune 1970, 1971; Boore 2003), where M_0 is the seismic moment (in SI units), $\Theta_{\lambda\Phi}$ is the average radiation pattern $\Theta_{\lambda\Phi} = 0.55$ for S waves (Aki & Richards 1980; Boore & Boatwright 1984), v is the S-wave velocity at the source (it is assumed that $v = 3.5$ km s^{-1}), F is the free surface amplification ($F = 2.0$ for normally incident SH waves and a good approximation for SV) and ρ is the average crustal density ($\rho = 2800$ kg m^{-3}). r_0 is the fault radius. The apparent geometrical spreading function, $S(r)$ (Atkinson & Mereu 1992), which may include factors such as phase interference and dispersion, focusing or defocusing and scattering, is described by a piecewise function comprising segments of constant exponential

decay:

$$S_{ij}(r) = \begin{Bmatrix} \left(\frac{r_0}{r}\right)^{\lambda_1} & r_0 \le r \le r_1 \\ S(r_1) \cdot \left(\frac{r_1}{r}\right)^{\lambda_2} & r_1 \le r \le r_2 \\ \vdots & \vdots \\ S(r_n) \cdot \left(\frac{r_n}{r}\right)^{\lambda_n} & r \ge r_n \end{Bmatrix} \quad (26)$$

where r_0 is a reference distance before which apparent geometrical spreading is assumed to be zero to take into account the complexity of the rupture surface, that is, its deviation from a point source. $r_{i>0}$ are distances at which the geometrical spreading function segments. We may estimate r_0 using the source corner frequency and assuming a circular rupture plane.

$$r_0 = \frac{v_s k}{f_c}, \quad (27)$$

(Brune 1970, 1971). For shear waves, v_s is the shear wave velocity at the source, and k is 0.37 (Brune 1970, 1971). The parameter r_0 must also be used in the computation of the moment to restore the point source assumption; alternatively we may normalize the source size to $r_0 = 1$ km without affecting the moment or geometrical spreading value.

All 720 events were used in computing the rate of decay. In total 18 308 recordings were used (from either or both horizontal components). M_W values were taken from the Earthquake Catalogue of Switzerland (ECOS09). In a preliminary stage, a simple $1/r$ model without site terms was used to model all data. Plotting the residuals against distance and magnitude (Fig. 17) then indicates any further model complexity that is required. On average the $1/r$ model underestimates the rate of geometrical decay, leading to overestimation of the signal moment. More detailed inspection of the residual plot with distance shows that a trend is present, suggesting that the single rate of decay over the entire distance range is insufficient to model the data. A difference between Foreland and Alpine events is evident in the first 100 km, with different behaviour of residuals. Beyond around 150–200 km the decay sharply departs from the $1/r$ model. The plot of residuals relative to M_W shows that stronger decay is required for smaller events, although this can also be explained by the greater distances at which the larger magnitude events tend to be recorded.

To refine the geometrical decay model, a grid-search was performed over different segmentations distances (r_i). Site terms (A_j) were fixed to the values used for deriving the generic rock model (Poggi *et al*. 2011 and Fig. 18) and ECOS09 M_W were used. Table 6 and Fig. 19 show the best-fitting geometrical decay models. The best hypocentral distances for segmentation of the average model (both Foreland and Alpine data combined) were 70 km and 120 km, which are consistent with our expectations for the point at which *S*m*S* (Moho reflections) and Lg (trapped surface) waves begin to affect the observed energy field. This is similar to the model found by Bay *et al*. (2003). When limiting the data to Foreland only, a difference is seen with respect to the average model, with initial decay that is more rapid in the first 20 km, but weaker in the range

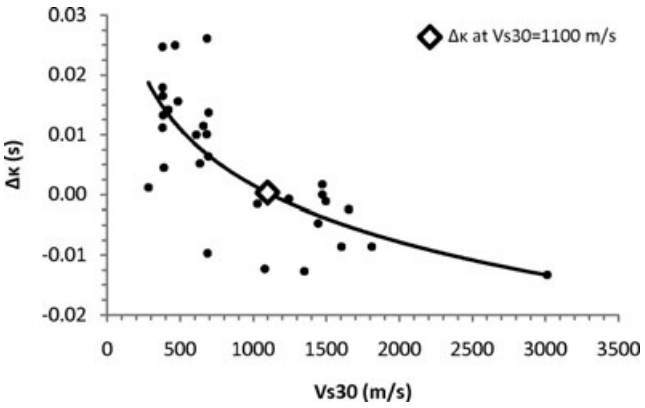

Figure 14. Plot of $\Delta\kappa$ versus measured V_s30 at selected Swiss Foreland sites. At $V_s30 = 1100$ m s^{-1}, consistent with the reference rock model, $\Delta\kappa = 0.00$ s. Station MUO was excluded from this plot.

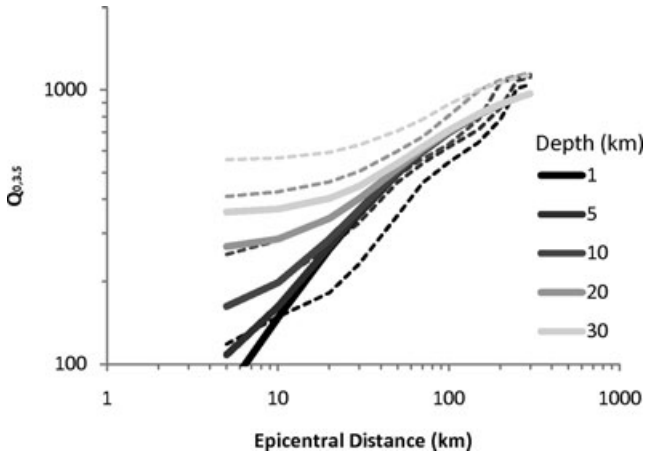

Figure 15. $Q_{0,3.5}$ plotted against epicentral distance for a range of source depths. The solid lines are from the homogeneous Q model with $\kappa = 0.016$ s, the dashed lines are from the 1-D Q model with $\Delta\kappa = 0.00$ s.

Table 5. Example t^* values computed from the 1-D Q and velocity model for a range of depths and epicentral distances.

		Source depth (km)							
	t^* (s)	1	2	4	5	10	15	20	30
Epicentral distance (km)	5	0.0073	0.0078	0.0074	0.0074	0.0077	0.0088	0.0094	0.0106
	10	0.0143	0.0142	0.013	0.0109	0.0093	0.0098	0.01	0.011
	20	0.0264	0.0249	0.021	0.017	0.0138	0.013	0.0125	0.0124
	30	0.0318	0.0299	0.0259	0.0214	0.0176	0.0167	0.0154	0.0142
	50	0.0359	0.032	0.0289	0.0261	0.0249	0.0233	0.0207	0.0185
	70	0.0387	0.0364	0.0345	0.0322	0.031	0.0294	0.0258	0.0229
	100	0.0474	0.0449	0.043	0.0411	0.0403	0.0355	0.0311	0.0286
	150	0.0614	0.0589	0.0568	0.0546	0.0498	0.0427	0.0384	0.0386
	200	0.0684	0.0661	0.064	0.0616	0.0488	0.0476	0.0478	0.0493
	250	0.0657	0.0642	0.0626	0.061	0.0594	0.0583	0.0586	0.0601
	300	0.0767	0.0753	0.0735	0.0719	0.0704	0.0693	0.0696	0.0709

20–140 km. The Foreland model could reflect the shallower Moho and deeper events in this region, with reflections being observed at shorter distances than in the Alpine. However, 20 km could be too soon for these *S*m*S* phases to be apparent as they should be observed at around twice the crustal thickness on average: in this case after 50 km. The Foreland model could be influenced by the recordings at less than 10 km in hypocentral distance. A number of problems can arise from these recordings. Small errors in source depth can significantly affect the apparent rate of decay, and the possibility of unmodelled near-source phenomena could affect results. These near-source data ($r < 10$ km) were removed and the geometrical decay recomputed. No significant change in the rates of decay was observed. The Alpine model was very similar to the average model, which is due to most of the data being classed as Alpine. The rate of decay for all models for distances greater than around 150 km was relatively uncertain, but it is always much greater than the expected $1/R^{0.5}$ decay of trapped surface waves. This is probably due to the dispersive behaviour of these surface waves, and the fact that the window length used for the computation of the FFT was limited to a maximum length of around 35 s, which may not be long enough to capture the complete Lg wave train. Fig. 17(b) shows the final residuals using the region-specific decay models given in Table 6, along with site terms (Poggi *et al*. 2011) plotted in Fig. 18. Overall, there are negligible trends in the misfit residuals for distance or magnitude (as opposed to using the simple $1/r$ model).

The geometrical decay model of Bay *et al*. (2003) is consistent with our findings for the average and Alpine models. They did not make any attempt to regionalize their model, so comparison of the Foreland model is not possible. The Bay model shows stronger Moho amplification effects in the 70–120 km range, although this could be a trade-off with their use of frequency-dependent Q (Morozov *et al*. 2008). Furthermore, they fixed the decay after 120 km to $1/R^{0.5}$, possibly due to limited noise-free data. The broad-band data in the new data set allows the resolution of the decay after 120 km, albeit with higher uncertainty than in the first 120 km. The theoretical value of $1/R^{0.5}$ for trapped surface waves is not reflective of the observations, even within the uncertainty. This is also similar to other studies (e.g. Frankel 1991; Edwards *et al*. 2008; Edwards & Rietbrock 2009). The higher than expected frequency-independent attenuation could be due to energy leakage into the mantle, in addition to the limited duration of the analysis window, meaning that coda-dominated signals at far distances are not completely accounted for.

Table 6. Rates of decay, λ, for the Foreland and Alpine models.

Dist. min.	Dist. max.	Foreland	Alpine	Average
1	20	1.29 ± 0.01	1.10 ± 0.00	1.11 ± 0.00
20	70	0.59 ± 0.03	1.10 ± 0.00	1.11 ± 0.00
70	120	0.59 ± 0.03	0.60 ± 0.05	0.41 ± 0.04
120	140	0.59 ± 0.03	0.60 ± 0.05	1.38 ± 0.05
140	160	1.02 ± 0.20	1.36 ± 0.11	1.38 ± 0.05
160	300	1.02 ± 0.20	1.36 ± 0.11	1.38 ± 0.05

11 DISCUSSION AND CONCLUSIONS

Attenuation of radiated shear wave energy from small earthquakes in Switzerland has been parametrized in terms of Q_0, κ and apparent geometrical decay. Two distinct models of analastic and scattering attenuation were presented: a simple layer-over-half-space model (Anderson & Hough 1984), using Q_0 and κ; and a 1-D $Q(z)_{\rm ref}$ profile, with the inclusion of lateral complexity through the definition of $\Delta\kappa$. It was shown that the model of Anderson & Hough (1984) is suitable up to around 250 km, with weak crustal attenuation ($Q_0 = 1216$) and comparatively strong near-surface attenuation ($\kappa = 0.016$ s at $V_s30 = 1100$ m s^{-1}). The use of a 1-D $Q(z)_{\rm ref}$ profile was also explored. Based on the reference velocity model adopted (Poggi *et al*. 2011) a Q profile that increased from around 200 at 1 km, to over 1000 at 20 km was found. Analysis of data from the Swiss Foreland region showed lower Q at depths of 1 km, but higher Q at depth. A parameter $\Delta\kappa$ was used to describe the lateral variation of attenuation relative to the average 1-D $Q(z)_{\rm ref}$ model. In the Foreland, $\Delta\kappa$ was higher, reflecting the stronger attenuation in the sedimentary deposits, whereas $\Delta\kappa$ was lower in the Alpine area, dominated by crystalline rocks.

The frequency dependence of Q was tested, it was found that using the model $Q(f) = Q_0 f^{\alpha}$, with $\alpha = 0.3$, led to a small reduction in the residual misfit when fitting the spectral shape. However, this model also resulted in a significant increase in the misfit of the apparent geometrical decay function. This may be due to the simplified $Q(f)$ model. Without a minimum $Q(f)$ value, and using $\alpha = 0.3$ leads to $Q(1\ {\rm Hz}) = 209$, with $\kappa = 0.005$ s following the model formulation of Anderson & Hough (1984). It is possible that the overattenuation of the low-frequency spectral plateau leads to this increase in the bias and misfit of the geometrical decay function. Morozov *et al*. (2008) found that using synthetic and nuclear explosion data, the frequency dependence of Q would be strongly overestimated, trading off with the geometrical decay. They suggested that it is better to model frequency independent Q, with allowance for variation in the geometrical decay, the approach we followed.

Attenuation of seismic energy is generally assumed to be due to a combination of intrinsic and scattering attenuation. In a

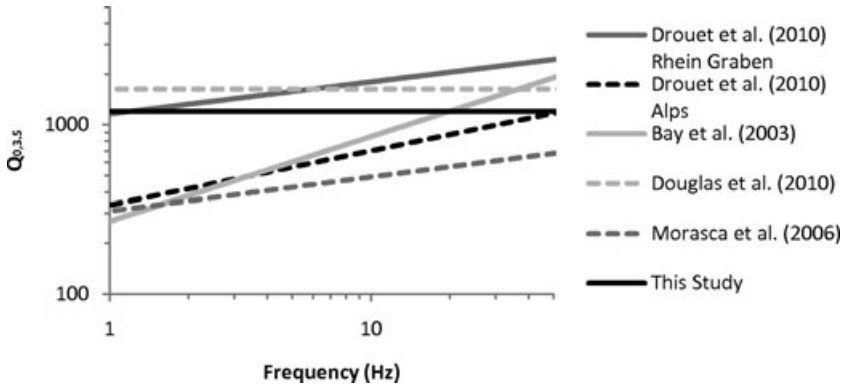

Figure 16. Comparison of attenuation functions [$Q(f)$] for the Switzerland and surrounding regions.

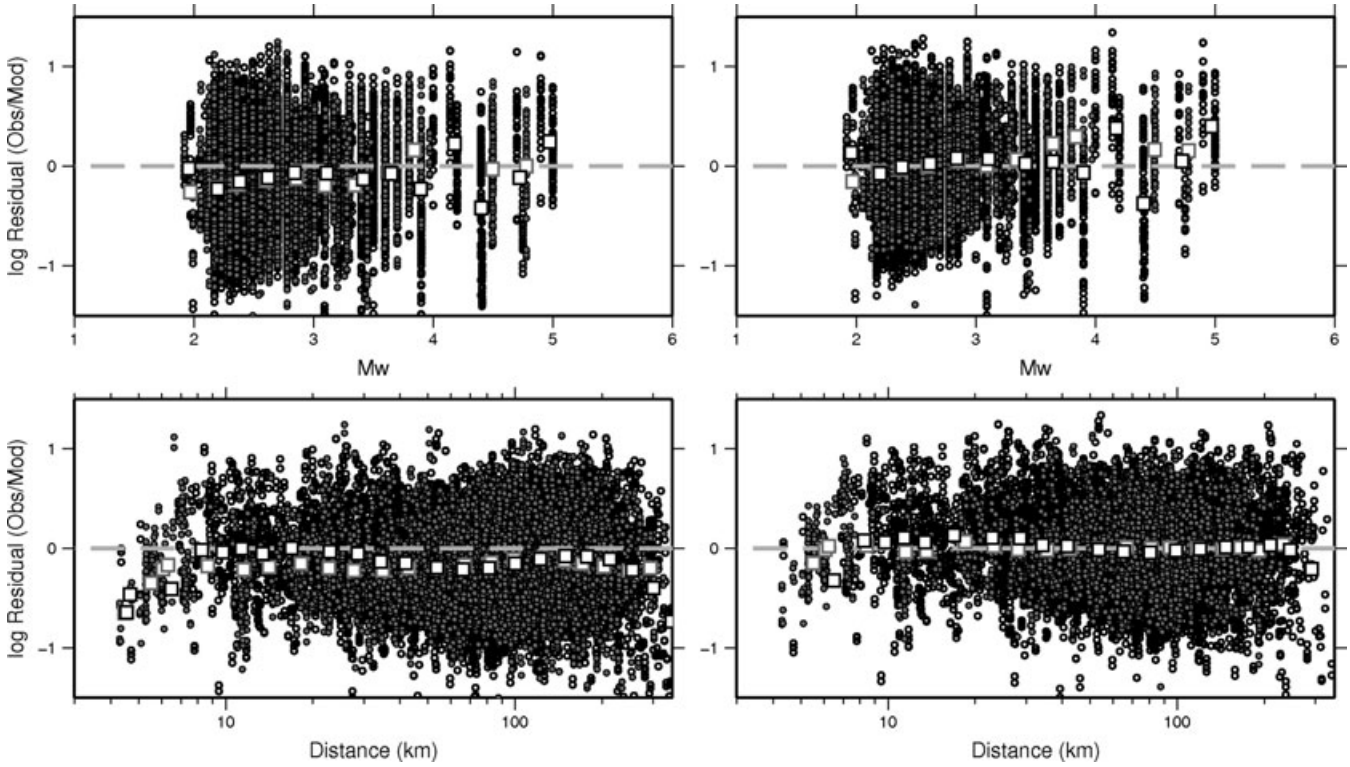

Figure 17. Residual analysis of signal moments relative to (a) $1/r$ decay model, (b) the specific Foreland and Alpine models (Table 6), using M_W from ECOS09 and site terms relative to the Swiss generic reference model (Poggi *et al*. 2011). Grey circles: Foreland events; black circles: Alpine events. Bottom panel: residuals plotted against distance (highlighting the departure from the decay model if present). Top panel: residuals plotted against magnitude. Squares (grey = Foreland, black = Alpine) show the mean residual at log-spaced distances and equally spaced magnitudes.

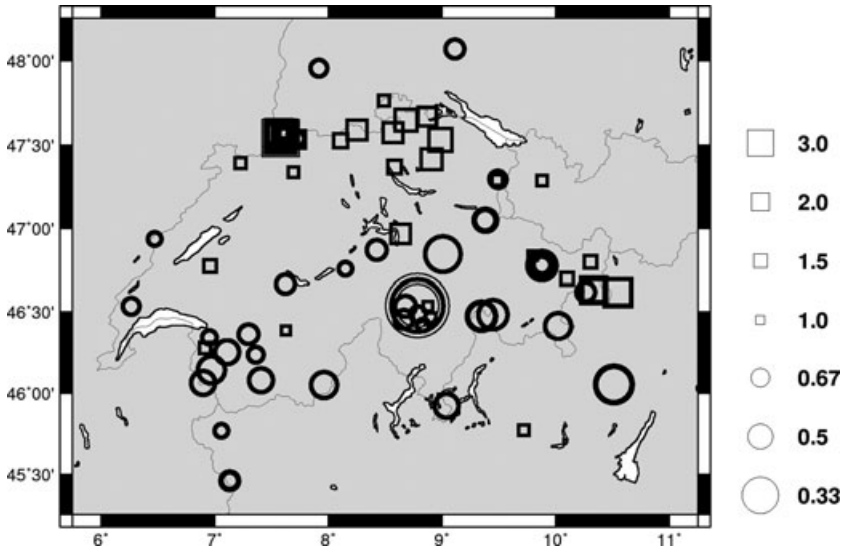

Figure 18. Site terms (from Poggi *et al.* 2011). Thick lines indicate mean amplitude (proportional to shape size), thin lines, if present, indicate uncertainty. Circles indicate deamplification, squares indicate average amplification relative to the Swiss generic rock velocity model.

review of Q models, Yoshimoto & Jin (2008) concluded that 'In general, Q_c^{-1} [$1/Q$ of the coda] lies between direct S-wave Q_S^{-1} [$1/Q$ of the direct S wave] and intrinsic absorption Q_{INT}^{-1} [$1/Q$ due to intrinsic absorption]'. These components of attenuation are difficult to separate, however, our analysis of Q over long (i.e. over 10 s) and very short (2.56 s) windows is consistent with this observation: on average, a decrease in Q was observed when using the short window lengths around the direct S wave with respect to those windows including coda. However, further work is required to quantitatively describe the contributions of intrinsic and scattering attenuation.

Modelling the apparent geometrical decay after accounting for the $Q(z)_{ref}$ and $\Delta\kappa$ model while using ECOS09 M_W, and site amplification of the reference velocity model given in Poggi *et al.* (2011), it was found that the average decay was close to spherical geometrical spreading, with $1/R^{1.1}$ in the first 70 km. Amplification of the low-frequency plateau was then observed in the region between 70 and 120 km (with $1/R^{0.4}$), attributed to *S*m*S* reflections.

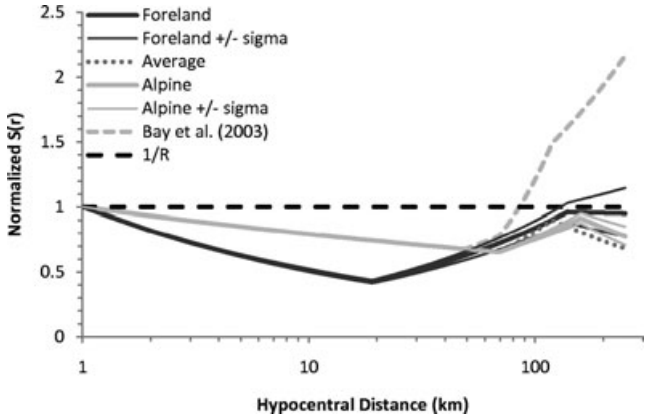

Figure 19. Geometrical spreading models normalized by a $1/R$ model.

Finally, the decay continued with $1/R^{1.4}$, significantly stronger than simple cylindrical spreading attenuation. This could be due to energy leakage into the mantle, in addition to the limited duration of the analysis window, meaning that coda-dominated signals at far distances are not completely accounted for. Nevertheless, as we are interested in the significant duration of shaking, accounting for the dispersion of the coda is not necessary. The analysis of Foreland and Alpine data showed strong differences in the regional decay functions. In the Foreland, the decay was initially stronger, albeit only until 20 km (with $1/R^{1.3}$), the Foreland region then exhibited amplification due to *S*m*S* reflection phases. On the other hand the Alpine region showed decay consistent with the average model. This is due to more data being recorded in the Alpine region. In the Alpine region *S*m*S* phase amplification was only observed after 70 km, later than in the Foreland. This is consistent with the deeper Moho in the Alpine region in addition to the shallower events. The decay at greater distances is roughly consistent between both regions, albeit within the larger uncertainty at this distance range.

The implementation of the attenuation models presented in this work is very much application specific. There are strengths and weaknesses in both the Q_0 and 1-D Q models. For instance, the 1-D model may better represent the change of Q with depth, and take into account factors such as source depth when computing t^*_{path}. Additionally, if Q varies with depth, the Q_0 model will overestimate attenuation in the near field, due to the use of κ independent of source distance. On the other hand, the 1-D model is not as simple to implement as the Q_0 model. One such example is the stochastic simulation software of Boore (2003), which requires values of Q_0 and κ. Given the similarities in the resultant t^*_{path}, and the difficulty in determining the better model, it would not necessarily we worthwhile implementing the 1-D Q model in this application.

ACKNOWLEDGMENTS

Some figures in this paper were produced using GMT 4 (generic mapping tools) software written by Wessel & Smith (1998). Fig. 1 was created by Sabine Wöhlbier. Parts of the code used in creating the inversion tools were provided by Pozo (2004) and Press *et al*. (1997). The tomography software simul2000 (Thurber 1983, 1993; Eberhart-Phillips 1993) was used for the 1-D Q models. For information regarding the Swiss seismic network see http://www.seismo.ethz.ch/networks/SDSNet/SDSNet.html. Further data were obtained from the German Regional Seismic Network (GRSN), the Austrian Seismic Network (ZAMG), the Italian Seismic Network (INGV), the French Accelerometric Network (RAP), the Mediterranean Broadband Seismic Network (MEDNET) and the Landeserdbebendienst Baden-Württemberg (LED). We extend our thanks to two anonymous reviewers and Editor Prof. Michael Korn for their helpful comments. This work was partly funded by *swissnuclear* within the Pegasos Refinement Project (Renault *et al*. 2010).

REFERENCES

Aki, K. & Richards, P., 1980. *Quantitative Seismology,* W. H. Freeman, New York.

Anderson, J.G. & Hough, S.E., 1984. A model for the shape of the Fourier amplitude spectrum of acceleration at high frequencies, *Bull. seism. Soc. Am.,* **74**, 1969–1993.

Atkinson, G.M. & Boore, D.M. 2006. Earthquake ground-motion prediction equations for eastern North America, *Bull. seism. Soc. Am.,* **96**, 2181–2205; doi:10.1785/0120050245.

Atkinson, G. & Mereu, R., 1992. The shape of ground motion attenuation curves in south-eastern Canada, *Bull. seism. Soc. Am.,* **82**, 2014–2031.

Bay, F.D., Malagnini, L. & Giardini, D., 2003. Spectral shear-wave ground-motion scaling in Switzerland, *Bull. seism. Soc. Am,* **93**, 414–429.

Bay, F., Wiemer, S., Fäh, D. & Giardini, D., 2005. Predictive ground motion scaling in Switzerland: best estimates and uncertainties, *J. Seismol.,* **9**, 223–240.

Boore, D.M., 2003. Simulation of ground motion using the stochastic method, *Pure appl. Geophys.,* **160**, 635–676.

Boore, D.M. & Boatwright, J., 1984. Average body-wave radiation coefficients, *Bull. seism. Soc. Am.,* **74**, 1615–1621.

Boore, D., Joyner, W. & Wennerberg, L., 1992. Fitting the stochastic ω-2 source model to observed response spectra in western North America: trade offs between $\Delta\sigma$ and κ, *Bull. seism. Soc. Am.,* **82**, 1956–1963.

Brune, J.N., 1970. Tectonic stress and the spectra of seismic shear waves from earthquakes, *J. geophys. Res.,* **75**, 4997–5010.

Brune, J.N., 1971. Correction: tectonic stress and the spectra of seismic shear waves from earthquakes, *J. geophys. Res.,* **76**, 5002.

BSSC, Building Seismic Safety Council 2003. *The 2003 NEHRP Recommended Provisions for New Buildings and Other Structures*. *Part 1: Provisions (FEMA 450)*, www. bssconline.org (last accessed 2011 March).

Chandler, A.M., Lam, N.T.K. & Tsang, H.H., 2006. Near-surface attenuation modelling based on rock shear-wave velocity profile, *Soil Dyn. Earthq. Eng.,* **26**, 1004–1014.

Cotton, F., Scherbaum F., Bommer J.J. & Bungum H., 2006. Criteria for selecting and adjusting ground-motion models for specific target regions: application to Central Europe and rock sites, *J. Seismol.,* **10**, 137–156.

Deichmann, N. *et al*., 2010. Earthquakes in Switzerland and surrounding regions during 2009, *Swiss J. Geosci.* **103**, 535–549.

Douglas, J., Gehl, P., Bonilla, L.F. & Gelis, C., 2010. A kappa model for mainland France, *Pure appl. Geophys.,* **167,** 1303–1315, doi:10.1007/s00024-010-0146-5.

Drouet, S., Cotton, F. & Guéguen, P., 2010. vS_{30}, κ, regional attenuation and M_w from accelerograms: application to magnitude 3–5 French earthquakes. *Geophys. J. Int.,* **182**, 880–898. doi:10.1111/j.1365-246X.2010.04626.x.

Eberhart-Phillips, D., 1993. Local earthquake tomography: earthquake source regions, in *Seismic Tomography: Theory and Practice,* pp. 613–643, eds Iyer, H.M. & Hirahara, K., Chapman and Hall, New York, NY.

Eberhart-Phillips, D., Chadwick, M. & Bannister, S., 2008. Three-dimensional attenuation structure of central and southern South Island, New Zealand, from local earthquakes, *J. geophys. Res.,* **113**, B05308, doi:10.1029/2007JB005359.

Eberhart-Phillips, D., McVerry, G. & Reyners, M., 2010. Influence of the 3D distribution of Q and crustal structure on ground motions from the 2003 M-w 7.2 Fiordland, New Zealand, Earthquake. *Bull. seism. Soc. Am.,* **100**, 1225–1240.

Edwards, B. & Rietbrock, A., 2009. A comparative study on attenuation & source-scaling relations in the Kanto, Tokai, & Chubu Regions of

Japan, using data from Hi-Net & Kik-Net, *Bull. seism. Soc. Am.,* **99**, doi:10.1785/0120080292.

Edwards, B., Rietbrock, A., Bommer, J.J. & Baptie, B., 2008. The acquisition of source, path and site effects from micro-earthquake recordings using Q tomography: application to the UK, *Bull. seism. Soc. Am.,* **98**, 1915–1935.

Edwards, B., Allmann, B., Fäh, D. & Clinton, J., 2010. Automatic computation of moment magnitudes for small earthquakes & the scaling of local to moment magnitude. *Geophys. J. Int.,* **183**, 407–420. doi:10.1111/j.1365-246X.2010.04743.x.

Eshelby, J.D., 1957. The determination of an elastic field of an ellipsoidal inclusion & related problems, *Proc. Roy. Soc. London A,* **241**, 376–396.

Fäh, D. & Huggenberger, P., 2006. INTERREG III, Erdbebenmikrozonierung am sülichen Oberrhein. Zusammenfassung fü das Projektgebiet Gebiet in der Schweiz. CD & Report (in German; available from the authors).

Fäh, D., Stamm, G. & Havenith, H.B., 2008. Analysis of three-component ambient vibration array measurements, *Geophys J. Int,* **172**, 199–213.

Fäh, D. *et al*., 2009. Determination of site information for seismic stations in Switzerland, Swiss Seismological Service Technical Report: SED/PRP/R/004/20090831, for the *swissnuclear* Pegasos Refinement Project.

Frankel, A., 1991. Mechanisms of seismic attenuation in the crust: scattering and anelasticity in New York State, South Africa, and southern California, *J. geophys. Res.* **96**, 6269–6289.

Hanks, T.C. 1982. fmax, *Bull. seism. Soc. Am.* **72**, 1867–1880.

Havenith, H.B., Fäh, D., Pollom, U. & Roulle, A., 2007. S-wave velocity measurements applied to the seismic microzonation of Basel, Upper Rhine Graben, *Geophys. J. Int.,* **170**, 346–358.

Ide, S., Beroza, G.C., Prejean S.G. & Ellsworth, W.L., 2003. Apparent break in earthquake scaling due to path and site effects on deep borehole recordings, *J. geophys. Res.,* **108**, B5, 2271, doi:10.1029/2001JB001617.

Lees, J.M. & Park, J. , 1995. Multiple-taper spectral analysis: a stand-alone C subroutine, *Comput. Geosci.,* **21**, 199–236.

Malagnini, L., Herrmann, R.B. & Koch, K., 2000. Ground motion scaling in central Europe, *Bull. seism. Soc. Am.* **90**, 1052–1061.

Mayeda K., & Malagnini, L., 2010. Source radiation invariant property of local and near-regional shear-wave coda: application to source scaling for the M-w 5.9 Wells, Nevada sequence, *Geophys. Res. Lett.,* **37**, L07306, doi:10.1029/2009GL042148.

Morasca, P.L., Malagnini, A., Akinci, D., Spallarossa & Herrmann, R.B., 2006. Ground-motion scaling in the Western Alps, *J. Seismol.,* **10**, 315–333, doi:10.1007/s10950-006-9019-x.

Morozov, I.B., Zhang, C., Duenow, J.N., Morozova, E.A. & Smithson, S., 2008. Frequency dependence of regional coda Q. Part I. Numerical modeling and an example from Peaceful Nuclear Explosions, *Bull. seism. Soc. Am.,* **98**, 2615–2628, doi:10.1785/0120080037.

Park, J., Lindberg, C.R. & Vernon, F.L. (1987). Multitaper spectral analysis of high frequency seismograms, *J. geophys. Res.,* **92**, 12 675–12 684.

Poggi, V. & Fäh, D., 2010. Estimating Rayleigh wave particle motion from three-component array analysis of ambient vibrations. *Geophys. J. Int.,* **180**: 251–267. doi:10.1111/j.1365-246X.2009.04402.x.

Poggi, V., Edwards, B. & Fäh, D., 2011. Derivation of a reference shear-wave velocity model from empirical site amplification, *Bull. Seis. Soc. Am.,* **101,** 258–274, doi:10.1785/0120100060.

Pozo, R., 2004. Template Numerical Toolkit. Available from: http://math.nist.gov/tnt/, Accessed May 2009.

Press, W.H., Teukolsky, S.A., Vetterling, W.T. & Flannery, B.P., 1997. *Numerical Recipes in C: The Art of Scientific Computing,* 2nd edn, Cambridge University Press, Cambridge.

Raoof, M., Herrmann, R.B. & Malagnini, L., 1999. Attenuation and excitation of three component ground motion in southern California, *Bull. seism. Soc. Am.,* **89**, 888–902.

Scherbaum, F., 1990. Combined inversion for the three-dimensional Q structure and source parameters using microearthquake spectra, *J. geophys. Res.,* **95**, 12 423–12 438.

Scherbaum, F., Cotton, F. & Staedtke, H., 2006. The estimation of minimum-misfit stochastic models from empirical ground-motion equations, *Bull. seism. Soc. Am.,* **96**, 427–445.

Silva, W., Darragh, R., Gregor, N., Martin, G., Abrahamson, N. & Kircher, C., 1998. Reassessment of site coefficients and near-fault factors for building code provisions, Technical Report Program Element II: 98-HQ-GR-1010, Pacific Engineering and Analysis, El Cerrito, USA.

Thurber, C.H., 1983. Earthquake locations and three-dimensional structure in the Cyote Lake area, central California, *J. geophys. Res.,* **8**, 8226–8236.

Thurber, C.H., 1993. Local earthquake tomography: velocities and vp/vs theory, in *Seismic Tomography: Theory and Practice,* pp. 563–583, eds Iyer, H.M. & Hirahara, K., Chapman and Hall, New York, NY.

Renault, P., Heuberger, S. & Abrahamson, N.A., 2010, PEGASOS Refinement Project: An improved PSHA for Swiss nuclear power plants, in *Proceedings of 14ECEE—European Conference of Earthquake Engineering,* Ohrid, Republic of Macedonia, Paper ID 991.

Rietbrock, A., 2001. P wave attenuation structure in the fault area of the 1995 Kobe earthquake, *J. geophys. Res.,* **106**, 4141–4154.

Toro, G.R., Abrahamson, N.A. & Schneider, J.F., 1997. A model of strong ground motions from earthquakes in central and eastern North America: best estimates and uncertainties, *Seismol. Res. Lett.,* **68**, 41–57.

Viegas G., Abercrombie, R.E. & Won-Young Kim, 2010, The 2002 M5 Au Sable Forks, NY, earthquake sequence: source scaling relationships and energy budget. *J. geophys. Res,* **115**, B07310, doi:10.1029/2009JB006799.

Wessel, P. & Smith, W.H.F., 1998. New, improved version of the generic mapping tools released, *EOS, Trans. Am. geophys. Un.,* **79**, 579.

Yoshimoto, K. & Jin, A., 2008. Coda energy distribution and attenuation: Earth heterogeneity and scattering effects on seismic waves, in *Advances in Geophysics,* Vol. 50, ch. 10, pp. 265–299, eds Dmowska & Renata, Elsevier, doi:10.1016/S0065-2687(08)00010-1.